



Carbon Export and Fate Beneath a Dynamic Upwelled Filament off the California Coast

Hannah L. Bourne¹, James K. B. Bishop^{1,2}, Elizabeth J. Connors^{1,3}, Todd J. Wood²

¹Dept. of Earth and Planetary Science, University of California, Berkeley, CA, 94720, USA

5 ²Earth and Environmental Sciences Division, Lawrence Berkeley National Laboratory, Berkeley, CA, 94720, USA

³Scripps Institution of Oceanography, La Jolla, CA, 92093, USA

Correspondence to: James K.B. Bishop (jkbishop@berkeley.edu)

Abstract. To understand the vertical variations of carbon fluxes in biologically productive waters, four autonomous Carbon Flux Explorers (CFEs) and ship-lowered CTD-interfaced particle-sensitive transmissometer and scattering sensors were
10 deployed in a filament of offshore flowing recently upwelled water during the June 2017 California Current Ecosystem – Long Term Ecological Research process study. The Lagrangian CFEs operating at depths from 100-500 m yielded carbon flux and its partitioning with size from 30 μm –1 cm at three intense study locations within the filament and at a location outside the filament. Different particle classes (anchovy pellets, copepod pellets and $>1000 \mu\text{m}$ aggregates) dominated the 100-150 m fluxes during successive stages of the filament evolution as it progressed offshore. Fluxes were very high at all locations in the
15 filament; below 150 m, flux was invariant or increased with depth at the two locations closer to the coast. Martin curve ‘b’ factors for total particulate carbon flux were +0.1, +0.87, -0.27, and -0.39 at the three successively occupied locations within the plume, and in transitional waters, respectively. Particle transfer efficiencies between 100 to 500 m were far greater within both filament and California Current waters than calculated using a classic Martin ‘b’ factor of -0.86. Interestingly, the flux profiles for all particles $<400 \mu\text{m}$ were a much closer fit to Martin; however, most (typically $>90\%$) of particle flux was carried
20 by $>1000 \mu\text{m}$ sized aggregates. Mechanisms to explain a factor of three flux increase between 150 and 500 m at the mid plume location are investigated.

1 Introduction

Carbon export driven by the biological carbon pump, the process by which photosynthetically derived biomass is transported out of the surface layer, is an important component of the global carbon cycle. Atmospheric carbon concentrations are in part
25 controlled by the depth at which sinking organic matter is remineralized (Kwon et al., 2009) yet the fate of carbon exported to deeper waters beneath highly productive coastal regions is poorly understood. Current estimates for carbon export range from 5 to $>12 \text{ Pg C yr}^{-1}$ (Boyd and Trull, 2007; Henson et al., 2011; Li and Cassar, 2016; Dunne et al., 2005; Siegel et al., 2014, 2016; Yao and Schlitzer, 2013). Because coastal upwelling regions are such productive and unique ecosystems with complex current interactions, a question to be asked is: “Is export of material to depth in these systems different than in open ocean



30 environments?”. If so, knowing the rules governing particulate carbon export and remineralization in these regions will significantly advance carbon cycle simulations of CO₂ uptake by the oceans.

While ocean color satellites provide temporal and spatial scale of phytoplankton biomass when clouds permit, flux beneath the euphotic zone is much more difficult to observe and therefore not as well known. A number of recent studies have noted discrepancies in reconciling meso- and bathypelagic activity with current euphotic zone flux estimates (Banse, 2013; Burd et al., 2010; Ebersbach et al., 2011; Passow, 2012; Stanley et al., 2012). Measurements of new production (NP, Eppley and Peterson, 1979) should balance particle export measured at the same time if gravitational particle sinking dominates export; however, NP often is higher than particle export (Bacon et al., 1996; Estapa et al., 2015; Stukel et al., 2015). Mechanistic understanding of these differences is thus important to food web models.

The strength and efficiency of the biological carbon pump is governed by complex interactions between phytoplankton, zooplankton and physical mixing. The Martin Curve (Equation 1), an empirical relationship, was derived from surface tethered sediment trap observations made in the north Pacific during the VERTEX program (Martin et al., 1987),

$$F = F_{\text{ref}} \left(\frac{z}{z_{\text{ref}}} \right)^b \quad (1)$$

45 where F is flux at depth z ; F_{ref} is the flux measured at a reference depth z_{ref} (usually near the base of the euphotic zone) and b is a constant. Martin et al. (1987) found best fits with $b = -0.86$ and $z_{\text{ref}} = 100\text{m}$.

Bishop (1989) compared the Martin and 6 other formulations for particle flux at depth in the open ocean and found that the Martin Curve for predicting flux was most robust; while many profiles were fit with the classic Martin “ b ” factor of -0.86 , the study found (in rare cases) b values of -0.3 to -1.5 . Subsequent studies in the open ocean have yielded similarly varying b values, and all show the expected flux decrease with depth (Fig. 1) (Buesseler et al., 2007; Lutz et al., 2007; Marsay et al., 2015).

If all material collected at depth in sediment traps is assumed to be gravitationally exported material originating from a stable photosynthetically derived source in the euphotic zone, an increase of material with depth should not occur. However, flux profiles that do not decrease monotonically with depth have been observed, especially in regions that are both physically and biologically dynamic, e.g. a seasonal study conducted between 2011 and 2013 in the Santa Cruz Basin (Bishop et al., 2016) and the summer of 2009 in the North Atlantic preceding the spring bloom (Giering et al., 2017), suggesting other processes are at play.

The California Current is an eastern boundary current at the edge of the North Pacific gyre that flows south from the sub-arctic North Pacific. Beneath it, the subsurface California Undercurrent flows north at depths between 200 and 500 m, with strong



60 seasonal variability (Lynn and Simpson, 1987). Along the coast, the complex interactions of filaments, geostrophic flow, wind-
driven Ekman transport and mesoscale eddies distribute coastal waters. This leads to a heterogeneous pattern of productivity
in surface waters with some regions having high productivity levels due to coastal upwelling, while others have intermediate
productivity spurred by wind stress curl upwelling or low productivity in more oligotrophic waters brought into the coastal
region through mesoscale processes and Ekman transport (Gruber et al., 2011; Ohman et al., 2013; Siegelman-Charbit et al.,
65 2018). In the summer, winds blowing south along the coast cause surface waters to divert to the west, which allows deep
nutrient rich cold water to come to the surface. This water coming to the surface moves out to sea in filaments which can
develop and extended offshore several hundred kilometers.

The California Current Ecosystem Long-Term Ecological Research (CCE-LTER) process study (June 1 - July 2 2017) gave
us the opportunity to observe carbon flux profiles beneath a rapidly evolving surface filament in an upwelling coastal
70 environment, and to understand the magnitude, scales and mechanisms of coastal production and its transport (Fig. 2). Carbon
Flux Explorers (robotic Lagrangian floats which image sinking particles, described in Bourne et al., 2019 and Bishop et al.,
2016) were deployed at various depths to 500 m to record particle flux, its variability and particle classes contributing to flux
over the lifetime of a productive filament.

Figure 2 shows the locations of CFE deployments during the 2017 CCE-LTER process study (P1706), the Santa Cruz Basin
75 (SCB) study site of Bishop et al., (2016) as well as the coastal station VERTEX 1 (Martin et al., 1987). The CCE-LTER
involved a combination of spatial surveys, three cross-filament CTD transects, and four sequentially-numbered multi-day
quasi-Lagrangian intensive sampling “cycles” at key locations within and outside of the filament. Cycles 1 to 4 correspond to
locations 1 to 4 which are referred to as L1 to L4 below.

In this study, we report observations of vertical profiles of carbon flux in the upper 500 m of a filament of upwelled water off
80 the coast of California and the finding at two locations that flux was invariant or increasing with depth, while flux decreased
slowly at two other locations. We explore reasons for the flux profile observations. In the following discussion, we use the
term “non-classic” to represent strong departures from the classic ($b=-0.86$) Martin curve.

1.1 Study Area

In June 2017, we participated in the CCE-LTER process study (P1706) aboard the R/V Revelle which followed a strong
85 filament of upwelled cold, high salinity westward flowing water off the coast of California. The filament developed during the
first week of June off Morro Bay (35°22' N and 122°52' W, (Fig. 2). In late May, cold water upwelled along the coast due to
the intensification of winds blowing north to south along the coast (Fig. 3 a,b). By the first week of June, the recently upwelled
water was flowing in a filament out into the Pacific (Fig. 3 c,d). By mid-June, the end of the filament had developed into a
cyclonic eddy, becoming pronounced by the end of June as evident in maps of sea surface height (Fig. 4). Two pairs of CFEs
90 were deployed at each of four locations (Figs. 1 and 3), whereupon the CFEs drifted and were recovered before the next



deployment. These are detailed below. The locations are numbered sequentially according to deployment dates, with three (L1, L2 and L4) within the filament, and L3 in transitional waters just outside of the filament.

2. Methods

2.1 Remote Sensing Data

95 Sea surface temperature (SST), sea surface chlorophyll (Fig. 3), and euphotic zone depth were downloaded from NASA Ocean Color in 4 km, 8-day averaged resolution from the satellite VIIRS (Visible Infrared Imaging Radiometer Suite); MODIS Aqua data were also used. SMPP-VIIRS 4 km daily data were analyzed to provide a spatial context for L2. Coastal Zone Color Scanner data were analyzed to provide context for the June 1984 Martin et al. (1987) VERTEX 1 station. All NASA data were downloaded from (<https://oceancolor.gsfc.nasa.gov/l3/>). Sea surface height (SSH) data (Fig. 4) was downloaded from the
100 NASA Jet Propulsion Laboratory with 1/6th of a degree and 5-day resolution (<https://podaac.jpl.nasa.gov/>; doi: 10.5067/SLREF-CDRV1). The sea surface height data combined measurements from a suite of sensors.

2.2 Carbon Flux Explorer (CFE)

The CFE and the operation of its particle flux sensing Optical Sedimentation Recorder (OSR) have been discussed in detail in Bishop et al. (2016). Briefly, once deployed, the CFE dives below the surface to obtain observations at target depths as it drifts
105 with currents. The OSR wakes once the CFE has reached the target depth. On first wake-up of a given CFE dive, the sample stage is flushed with water and images of the particle-free stage are obtained. Particles settle through a 1-cm opening hexagonal celled light baffle into a high-aspect ratio funnel assembly before landing on a 2.54 cm diameter glass sample stage. At 25-minute intervals, particles are imaged at 13 μm pixel resolution in three lighting modes: dark field, transmitted and transmitted-cross polarized.

110 We focus on light attenuation proxy of carbon flux in this paper because the proxy has been calibrated in terms of carbon and nitrogen fluxes (Bourne et al., 2019). Particles build up sequentially during the imaging cycle over 1.8 hours until after a predetermined number of image sets are completed, at which time another cleaning occurs and a new reference image set is obtained; the process repeats. After ~ 6 h at a target depth, the OSR performs a final image set, cleaning cycle and reference image set, and the CFE surfaces to report GPS position, CTD profile data and OSR engineering data, and then dives again.

115 A total of four CFEs were deployed in this study. Two CFEs, referred to here as CFE-Cals (CFE-2 and CFE-4), were built to collect calibration samples as described in Bourne et al. (2019). These new CFEs were built with SOLO-II floats, which have a threefold greater buoyancy adjustment capability than the older CFEs (CFE-1, and CFE-3) which could not carry the samplers. CFE-Cals were programmed to drift at 150 m and were typically deployed twice for 24-hour deployments at each location. We found that the concave bladder housing of the SOLO-II float trapped air and made it more difficult for the CFE-



120 Cals to attain a stable target depth. This problem became an issue when the CFEs were launched in calm conditions. Subsequently, the CFE-Cal SOLO II bladder assembly was flushed with water before deployment and deployed horizontally to minimize the issue. The two other CFEs, CFE-1 and CFE-3, were programmed to drift at three depths (CFE-1 and 3 are referred to as profiling CFEs). At L1, bottom depth was ~450 m and we limited CFE dives to shallower than 300 m. At offshore locations L2, L3 and L4 the three target depths were 150, 250 and 500 m. The profiling CFEs (CFE-1 and CFE-3) were
125 deployed at each location for 3 to 4 days. At L3 outside the filament, CFE-3 relayed profile information but all imagery was lost as it was attacked twice violently by a charging 300 kg short-fin Mako shark as we watched. The first high velocity charge hit the OSR directly and had no effect on the CFE; the second charge hit the SOLO top cap and antenna assembly and broke the float causing CFE-3 to sink in seconds. Consequently, only CFE-1 made flux observations at L3 and L4 at 250 and 500 m. We deployed CFEs 24 times; 21 yielded results reported here (Table 1); 2 early deployments of CFE-Cals were not
130 useful, and CFE-3 was lost to a shark attack.

2.2.1 Reduction of OSR Transmitted Light Images

Sample attenuation calculation. Transmitted light color images were normalized by an in-situ composite image of the clean sample stage following Bishop et al. (2016) yielding a map of fractional transmission corrected for inhomogeneities of the light source. Attenuance (ATN) values were then calculated by taking the $-\log_{10}$ of the normalized image using the green color
135 plane. Pixels with an attenuation value less than 0.02 attenuation were defined to be background. Pixels above the threshold were integrated across the sample stage then divided by total number of pixels in the sample stage area to yield attenuation (ATN). ATN is then multiplied by 1000 to yield mATN. Figure 5 depicts time series of sample attenuation with depth at the mid-filament location L2; similar data from L1, L3 and L4 are shown in Appendix A, Figs. A1, A2 and A3, respectively. The figure illustrates attenuation increase over the course of an image cycle as more particles load onto the imaging stage and the
140 effect of cleaning which removes the particles and bring attenuation back down to baseline. Multiplying attenuation by the sample stage area (5.07 cm^2) gives sample Volume Attenuance (VA, units: $\text{mATN}\cdot\text{cm}^2$). Spatial context for CFE deployments, drifter and sediment trap deployments, and CTD casts, along with remotely sensed chlorophyll is also provided in the figures.

2.2.2 Calibration of POC_{ATN} to POC

Volume Attenuance (VA) has been calibrated in terms of particulate organic carbon and nitrogen (POC and PN) flux, as
145 detailed in Bourne et al (2019). Briefly, during cleaning, imaged particles were directed to sample bottles. The sample bottles were then filtered and analyzed for carbon and nitrogen. Regressions of VA to POC and PN concentrations results yielded slopes of $10,070 \text{ mATN}\cdot\text{cm}^2$: mmol POC ($R^2=0.86$) and $100,500 \text{ mATN}\cdot\text{cm}^2$: mmol PN ($R^2=0.87$). The regression was found to be robust in all regimes sampled even though there were variations in total particle abundance and dominant size fractions at each location. The conversion factor for VA:POC when transformed to flux units is $1.03 \text{ mATN}\cdot\text{cm}^2 \text{ cm}^{-2} \text{ d}^{-1}$ per mmol C
150 $\text{m}^{-2} \text{ d}^{-1}$ ($R^2=0.87$).



2.2.3 Particle Size Distributions

Three methods were used to determine particle size distributions in CFE imagery: (1) A computationally fast code that measures particle area and attenuation (Bourne, 2018), (2) manual identification and counting of particle classes, and (3) a hybrid of image analysis and visual verification of identified particles. Both methods 1 and 3 (after modification) would be possible to run on the CFE during deployment and are described in more detail below.

Transmitted light images from the CFEs were processed to attenuation units following Bishop et al. (2016). Results were saved as imagery in attenuation units where counts in each 8-bit (red, green, blue) color plane are scaled so that 100 counts = 1 attenuation unit. Approximately 1600 CFE attenuation images and corresponding transmitted light images from which attenuation was derived are available through the Biological and Chemical Oceanography Data Management Office (BCO-DMO) and Woods Hole Oceanographic Institution (Bishop, 2020a).

For size analysis, the RGB image is converted to an 8-bit grayscale image. We note that the 5 Mpixel SUMIX imager used in the CFE employs a Bayer filter in a checkerboard pattern that allocates 50% of the pixels to green (e.g. all the black diagonal squares on the board) and 25% to each of the blue and red color channels (non-black squares on alternate rows). In the case of transmitted light imagery, we have found little difference in attenuation values from the three color planes (Bourne et al. 2019); however, this is not true of imagery in dark field illumination. We choose to set the definition of a “particle” as having 4 contiguous pixels above threshold in order to provide compatibility with interpretation of darkfield imagery (now in progress), where color is important.

Method 1. Threshold variation.

Bourne (2018) developed a fast nearest-neighbor particle detection algorithm to measure attenuation size distribution in CFE images that is possible to run while the CFE is deployed. This was an important first step towards fully autonomous observations. Unlike the ‘stage’ integration method in Sect. 2.1.1, particle size analysis requires a choice of an attenuation count threshold to distinguish particles and differentiate them from background. Choosing too low of a threshold can increase the false detection of particles due to imperfections of lighting and sensor noise.

In this method, as well as Method 3, particle size distributions were determined in the last image of a cycle before the imaging stage was cleaned. If overlapping particles were present, the previous image in the series would be used instead. This choice was made manually, but could be implemented computationally.

Thresholds were varied from 0.02 to 0.20 attenuation units. Even at the highest threshold setting, the method failed in the case of touching ovoid fecal pellets (Fig. 6) which constituted a significant component of particle flux at 150 m at L2. Bourne (2018) used 0.12 to systematically explore the sample set. In the hybrid Method 3 below we use a threshold of 0.04. A total of 143 image cycles were analysed using this method.



Method 2. Manual Counting

CFE images from L2 were manually enumerated for ovoid fecal pellets and >1000 μm sized aggregates using a combination of transmitted light and darkfield imagery (Connors et al., 2018; Bourne et al. 2019).

Method 3. ImageJ size analysis and secondary processing

185 In Method 3, the software package ImageJ 1.52 (IJ, National Institutes of Health) was used for particle size analysis. The
advantage of ImageJ is that output results include a rich statistical description of the individual particles that can aid in particle
class analysis. In this method, we manually inspected the 4 to 5 sequential attenuation images taken during a two-hour long
image cycle to determine the point of onset of particle overlap. The image at this point was subtracted from the image of the
clean sample stage taken immediately preceding the image set. A threshold of 4 counts and above was used to define the
190 presence of particles (2 counts higher than used for calculation of VA) to facilitate particle identification. At this threshold
setting, large aggregates were fully detected; however, touching particles – particularly 200-400 μm sized fecal pellets (Fig.
6) were not separable. Each IJ-identified “particle” with multiple units was counted and these counts assigned to its sequence
number. Inspection of the imagery also identified touching aggregates which were similarly treated. During secondary data
processing, the area of each multi-unit “particle” was divided by the number of subunits, and its particle number was changed
195 from 1 to the determined count. Living organisms rarely appeared in images; when they did appear, we were able to identify
pteropods, amphipods, copepods, siphonophores, acantharia, radiolaria, and foraminifera. These, identified living particles
were removed from the secondary processed data. Total particle attenuation (average particle attenuation times particle area)
and particle number were binned into 65 logarithmically spaced size categories from (30 μm to 20000 μm). A total of 267
image pairs were analysed; combined flux results for each of 89 CFE dives are available online through the Biological and
200 Chemical Oceanography Data Management Office (BCO-DMO; Bishop, 2020b).

Data from each image cycle were weighted by the total number of images in that cycle; data from the multiple imaging/cleaning
cycles during a dive were binned and weighted by the duration of each imaging cycle. The particle attenuation and number
size-binned data were scaled to convert results to flux units ($\text{mATN-cm}^2 \text{ cm}^{-2} \text{ d}^{-1}$; and number $\text{m}^{-2} \text{ d}^{-1}$). The partitioning of
particle flux was further broken into 30-100, 100-200, 200-400, 400-1000, and >1000 μm categories. The 200-400 μm bin
205 primarily was populated by the numerous ovoid pellets. The >1000 μm bin was dominated by aggregates.

CFE attenuation images for all CFE deployments, and dive-averaged attenuation flux and number flux size distributions used
in this paper are archived in the Biological and Chemical Oceanography Data Management Office (BCO-DMO) at Woods
Hole Oceanographic Institution (Bishop, 2020).

Figure 7 displays normalized cumulative size distributions prior to and after secondary processing. The point of this labor-
210 intensive computer-aided approach is to provide a basis for future code development to enable fully autonomous particle size



distribution analyses aboard the CFE. The aim in this paper is to describe the number and attenuation fluxes of different sized particles and their changes down the water column during the CCE-LTER process study.

Figure 8 compares profiles of aggregate (>1000 μm) and pellet (200-400 μm) number fluxes with manually determined counts of these classes at location L2. Although the data were calculated in slightly different ways, Method 3 aggregate flux and manually determined aggregate flux closely matched. The Method 3 pellet flux agreed closely with manual counts at 150 m, but overestimated results at 500 m by a factor of 5. Average particle attenuation for all 150 to 400 μm sized particles at 150 m showed a cluster of particles >200 μm in size with attenuation values >0.25. These matched the ovoid fecal pellets. We calculated the ratio of the number of particles >0.25 attenuation to total particles and used the ratio to correct the Method 3 counts. Results brought the Method 2 and Method 3 counts at L2 into agreement. We applied this approach to L1, L3 and L4 data (Fig. 8). L4, in particular, showed high numbers of particles in the 200-400 μm category which originated from the fragmentation of large low attenuation aggregates; only 15% of particles had attenuation above 0.25 at 250 and 500m.

Figure A1-4 in Appendix A compares normalized-cumulative-attenuance flux and normalized-cumulative-number flux size-distributions from Methods 1 and 3 at locations (L1–L4). Some differences are attributed to independent choices of which image sets to analyse (137 vs. 267) using the two methods; never-the-less, we found good agreement between the methods for data from 250 m and deeper. The poorer agreement in size distributions from 150 m is due to the high threshold (0.12 attenuation) of Method 1 failing to detect large aggregates as whole particles and also the problem of touching fecal pellets, which dominated samples at 150 m at L2 (Fig. 6).

2.3 Acoustic Doppler Current Profiler (ADCP) and CTD data

Current velocity in u (east positive) and v (north positive) components from the hull mounted RD instruments 150 kHz narrow band Acoustic Doppler Current Profiler (ADCP) were averaged over 30-minute intervals during the times of CFE deployment. The 150 kHz data were limited to the upper 400 m. CFE drift velocities were also calculated based on CFE dive locations and times. Combined results are shown in Figure 9.

The hydrographic context for our study was provided by CTD profiles of T , S , potential density anomaly (σ_θ), and photosynthetically active radiation (PAR). In addition the CTD also carried particle concentration sensors for fluorescence (Seapoint Inc.), turbidity (Seapoint Inc.) and transmissiomiission (WETLabs, Inc. Philomath, OR). Protocols for particle optics are detailed in Bishop and Wood (2008). Daily CTD/Rosette deployments were typically made at 2 AM, 11 AM, and 6 PM (local time) in close proximity to a surface tethered drogued productivity array which served as the Lagrangian reference for studies at each location. Transmissometer derived beam attenuation coefficient (m^{-1}) was scaled by a constant factor of 27 to units of particulate organic carbon (POC) concentration (μM ; Bishop and Wood, 2009). Seapoint fluorescence data (an indicator of Chlorophyll) were offset by subtraction 0.05 units and were determined to be below detection at 0.02 units. Profile data were averaged over 10 seconds. The CTD also carried a UVP5-hd in-water particle imaging system (Hydroptic, France)



capable of resolving particles $>64 \mu\text{m}$ in reflected light. Data are available at <https://ecotaxa.obs-vlfr.fr/part/> Project: UVP5hd CCE LTER 2017. UVP data from individual CTD profiles averaged over 5 m intervals represents particles present in $\sim 180 \text{ L}$ and did not reliably sample the larger rare particles. We combined and depth-averaged all CTD cast data for each location to yielded particle size distributions from an equivalent water volume of $\sim 2000 \text{ L}$. We focus on particles $>1000 \mu\text{m}$ in size. Detailed analyses of UVP5 results beyond profile number abundance systematics, is beyond the scope to the paper. Samples from the CTD Rosette deployments at 2 AM and 11 AM each day were collected for nutrient analysis. All CTD/Rosette data are available from the CCE LTER data repository (<https://oceaninformatics.ucsd.edu/datazoo/catalogs/ccelter/datasets>).

3. Results

250 3.1 Water column environment

Figure 10 shows time series of T, S, potential density (σ_θ), chlorophyll fluorescence, transmissometer-derived POC and turbidity. We reordered the time axis to make data from in-filament locations L1, L2 and L4 more logically related and separate from the out-of-filament transitional waters observed at L3. L2 is split temporally into L2a and L2b for reasons outlined below. POC and Salinity – potential density transects are shown in Figure 11 along with POC / Salinity – potential density time series at the 4 locations. Time averaged profiles for T, S, potential density, beam attenuation coefficient, and nitrate at each location are shown in Fig. 12.

3.1.1 Location 1

L1 was closest Morro Bay and centered over a 50 km wide 500 m deep trough (Fig. 2). Upwelling was active as evidenced by surface waters of high salinity and low stratification (Fig. 10, 12). Here, CFE-1 and CFE-3 were deployed for 3 days from June 10–12; CFE-Cal's 2 and 4 were deployed for 18-20-hour periods twice during that time.

ADCP current results (Fig. 9a) show strong tidal fluctuation; overall, there was a net transport of water toward the southwest at a velocity of 0.06 m s^{-1} in the upper 50 m, 0.02 m s^{-1} between 100 and 200m, and 0.04 m s^{-1} between 200 and 300m.

The 24-hr mixed layer depth (MLD_{24}), defined by a potential density increase of 0.05 relative to surface values (Bishop and Wood, 2009), averaged 19 m (range from 13 to 25 m); euphotic zone depth was the same as MLD_{24} (21 m based on MODIS Aqua 8-day average data; $16 \pm 4 \text{ m}$ based on daytime CTD PAR sensor profiles where light was 1% of shallowest reading). The phytoplankton community was quickly growing and dissolved mixed-layer nitrate dropped from 10.2 to $5.4 \mu\text{M}$. The base of the euphotic zone corresponded to the $\sigma_\theta 25.5$ isopycnal. The SMPP-VIIRS chlorophyll map (Appendix A Fig. A-1(b)) shows that the deployments took place quite close to a very high chlorophyll waters.



3.1.2. Location 2

270 CFE-1 and CFE-3 were deployed from June 14 to 17. At L2, the water-column had begun to stabilize and stratify as evident by the thermocline and halocline (Fig. 11). MLD₂₄, averaged 26 m and ranged from 18 to 36 m. The euphotic depth was similar (29m MODIS Aqua; 25±3 m from PAR sensor profiles). The base euphotic zone was no deeper than the σ_{θ} 25.5 isopycnal. Euphotic zone salinity averaged ~33.70 PSU.

275 At most locations, the Lagrangian CFEs operated fairly close to locations of CTD profiles (Fig. 1). However, at L2, CFE-1 and CFE-3 were launched in a fast-moving jet and transported to the WNW (Fig. 5), the first deployment of CFE-Cals 2 and 4 tracked on a parallel course to CFE-1 and CFE-3. Their motion was away from the path traced by the productivity drifter – drogued at 15 m (Fig. 5b). When redeployed a day later near the drifter, CFE-Cals 2 and 4 advected to the west but at a greatly reduced speed indicating that the surface waters had become decoupled from the faster flow tracked by CFE-1 and CFE-3.

280 The temperature and salinity profiles from CFE-1 and CFE-3 were in close agreement with CTD casts 25-30, whereas the subsequent CTD cast data diverge. The first six CTD casts revealed a stronger halocline and pycnocline, with saltier, denser waters between about 25 and 150 m, indicating upwelling in this part of the timeseries. We thus treat the first 6 CTD casts as representative of CFE deployment 2a, and subsequent casts as 2b. In Figures 10 and 11, the hydrographic profiles for L2 are split temporally as L2a and L2b. By 200m depth, the salinity and density of all CTD casts converge (Fig. 12). Averaged nitrate in the upper 20 m was 8.6 μM and 7.8 μM during 2a and 2b, respectively.

285 During CFE deployments at L2a, ADCP velocity data show a net water flow toward the west-north-west at a velocity of 0.17 m s^{-1} in the upper 50 m, an increase to 0.29 m/s between 100 and 200m, and slight decrease to 0.27 m s^{-1} between 200 and 300m; at 500 m velocity was 0.15 m s^{-1} based on CFE motions. During L2b deployments, the current direction was westward but velocities were reduced at all depths (0.04 m s^{-1} in the upper 50 m, 0.11 m s^{-1} between 100 and 200m, and 0.12 m s^{-1} between 200 and 300m). Figure 5(b) shows the chlorophyll fields were quite uniform during deployments.

290 3.1.3 Location 3

This region was located in transitional waters between the westward extending filament and the surrounding waters of the California Current. CFE-1 and CFE-3 were deployed June 19–22. Unlike most locations, CFE-1 was deployed a second time about 10 km to the southeast (Figure 1). CFE-3 was lost due to a shark attack on June 20. CFE-Cals 2 and 4 were deployed twice for 20-hour periods. The MLD₂₄ at L3 averaged 27 m (range 11–69 m). The euphotic zone was at least twice as deep as
295 the MLD₂₄ (77 m NASA VIIRS; 49±7 m from PAR profiles).

Salinity of the upper 50 m at L3 decreased over time from 33.35 to less than 33.2 PSU indicating an increasing component of the southerly-flowing low-salinity California Current water (Schneider, et al., 2005). Surface layer (upper 20 m) dissolved nitrate from the midday cast on June 19 was 3.4 μM and decreased over 48 hours to 0.3 μM ; averaged nitrate at L3 was



1.5 μM . The euphotic zone was shallower than the $\sigma_\theta = 25.75$ isopycnal. Appendix A Fig. A-3(b) provides spatial context for
300 the observations and shows that the early deployments at L3 took place close the edge of the filament.

Current flow was to the southeast at L3 with faster velocities in the upper 50 m (0.30 m s^{-1}) compared to deeper waters (0.14 m s^{-1} between 100 and 200m, and 0.08 m s^{-1} between 200 and 300m). CFE drift at 500 m was 0.07 m s^{-1} .

3.1.4 Location 4

This site was located north of L3 in the western edge of the filament (Fig. 3 g,h). Based on the salinity signature of L2b and
305 L4, the water masses were similar (Fig. 12). By the time of CFE deployment at L4, between June 24 and 26, the filament
signature had begun to disappear, as can be seen in satellite chlorophyll (Fig. 3 g; Appendix A, Fig. A-1b), surface nutrients
were depleted, and sea surface temperature had increased due to solar heating (Fig. 3 h, Fig. 12). MLD_{24} averaged 9 m (range
5–14 m); euphotic depth was 51 ± 6 m from PAR profiles.

Average nitrate in the upper 20 m was $3.2 \mu\text{M}$. Water slowly advected to the northeast at 0.11 m/s in the upper 50 m, 0.04 m
310 s^{-1} between 100 and 200m, and at 0.02 m s^{-1} between 200 and 300 m; at 500 m CFE drifted at a velocity of 0.03 m s^{-1} . The
euphotic zone was bounded shallower than the $\sigma_\theta = 25.0$ isopycnal. Salinity of the upper layer was ~ 33.6 PSU.

A reasonable assumption is that the properties of surface water (here defined as upper 20 m) at L2 and L4 is a result of binary
mixing of recently upwelled L1 water with offshore California Current water at L3. Using L1 as the upwelled water end
member, and L3 as the offshore water end member, mixture proportions for L2 and L4 were calculated. L2a was a mixture of
315 81.1% upwelled water and 18.9% offshore water. L2b was a mixture of 80.9% upwelled water and 19.1% offshore water. L4
was 74% upwelled water and 26% offshore water. As the filament moved further offshore, the recently upwelled surface waters
mix progressively with offshore water (Fig. 12). The SMPP-VIIRS chlorophyll map (Appendix A, Fig. A-3(b)) shows little
variability in the vicinity of observations.

3.2 Sinking Particle Lateral Displacements

320 One of the questions raised in particle flux measurement is how representative of processes in the surface water is the vertical
flux data down the water column. As an exercise we consider particles sinking at a hypothetical rate of 100 m d^{-1} from 50 m
to depths of 150, 250, and 500 m and their lateral displacements during sinking at the 4 locations. Figure 13 visualises such
displacements.

CFE positions followed a near linear trajectory in time at many locations despite drifting at different depths. This allows a
325 simple calculation of displacements in the direction of motion. At L1, ADCP velocity data (discussed in Sect. 3.1) indicate
that particles sinking at 100 m d^{-1} would have lagged behind the surface layer by approximately 7 km as they transited from
50 m to 300 m.



At L2a, particles leaving 50 m would lead the motion of the surface layer by 11 km over the one day required to reach 150 m, a further 8 km lead would take place by 250 m; but particles would lag surface waters by 4.5 km as they sink from 250 m to 330 500 m. Taken together particles sinking from 50 m would have a net displacement of 15 km relative to the surface layer. At L2b, in a weaker current regime, sinking particles would lead the surface layer by 6 km during transit to 150 m, have a further lead by 6.5 km on reaching 250 m with a total displacement of 12.5 km by 250 m. We lack information for deeper waters as CFEs were not deployed deeper.

At L3, in transitional waters, particles would lag behind the motion of surface waters by 14 km on reaching 150 m, lag a further 335 distance of 19 km to 250 m, and 50 km more from 250 to 500 m for a total maximum displacement of 83 km.

At L4, Particles settling at 100 m d^{-1} would lag behind the 50 m layer by 3.5 km at 150 m, experience an additional 2 km lag by 250 m, and 7.5 km lag from 250 - 500 m for a total displacement of 13 km.

In summary, inferred lateral displacements were calculated relative to the direction of flow of surface waters as particles sink from 50 m to deeper waters. Smallest net displacements of sinking particles were found at L1 (7 km), L4 (13km) and L2a (15 340 km) with least displacement at L1 and at L4. Location L3 in the transitional waters had the strongest net displacements (83 km) making a 1D interpretation of particle flux most problematic at this location. An interesting feature of L2 is that particles at depth lead the surface layer (Fig. 13). Particle flux profiles sampled by the CFEs may reflect heterogeneous sources over the scales of displacement.

If spatial gradients of particle sources along the axis of the plume are weak, then the vertical lead and lag effects will be in 345 effect smaller. SMPP-VIIRS chlorophyll fields provide a measure of mesoscale chlorophyll variability at Location L2. Imagery from June 14 during the early stages of sampling show chlorophyll varying over a range of 3 to $1.75 \text{ mg Chl m}^{-3}$ along the path of the profiling CFE's; Imagery from June 17 showed a variation of 2.5 to $1.75 \text{ mg Chl m}^{-3}$ (Fig. 5b) along the same track. The two images for June 14 and 17, show ranges of 2.25 to 2.75 and 1.75 to $2.25 \text{ mg Chl m}^{-3}$, respectively in the vicinity of the later deployment of CFEs (waters referred to as L2b). If chlorophyll is a metric of particle flux, then spatially variable fluxes 350 would be expected to vary by less than a factor of two at L2. Similar maps for L1, L3 and L4 (Appendix Figs. A1-1, A1-2 and A1-3) indicate the likelihood of hererogenous fluxes at L1 and L3, but minimal heterogeneity at L4.

3.3 Particle Classes and CFE fluxes

Over the month of June as the filament advected to the west and aged, interactions with eastward flowing offshore waters led to the development of a cyclonic eddy (Fig. 4). Anti-cyclonic eddies formed both to the north and south of our sites. At all 355 locations, CFE trajectories closely matched ADCP velocities (Fig. 9) and the patterns of flow suggested by sea surface altimetry.



Figure 14 shows representative CFE imagery (selected from the 1250 images) taken at the 4 locations at depths 70, 125, and 250 m at L1, and at depths of 150, 250, and 500 m at the other locations. The dominant class of particles contributing to export at each location varied in the upper water column. Shallow export ~150 m at L1 was dominated by anchovy pellets; at L2 copepod pellets accounted on average for 50% of the flux (range 10% to 90%) with >1000 µm aggregates accounting for the rest (Fig. 14B). At L3 and L4 further offshore, export was dominated at all depths by >1000 µm sized aggregates. Large >1000 µm sized aggregates resembling discarded larvacean houses were common at all sites at depths 250 m and below. Such aggregates were also present in samples closer to the surface, though not typically as abundant.

Figure 15 shows Volume Attenuance Flux averaged for each dive during deployments at the 4 locations. Curves running through the data use Martin b factors derived from linear least squares fits to the log₁₀ transforms of the data represented by the form of Equation 2.

$$\log_{10}F = b \cdot \log_{10}(z/z_{\text{Ref}}) + \text{Log}_{10}(F_{\text{Ref}}) \quad (2)$$

F is CFE measured particle flux at depth z, and z_{Ref} was set to 50 m at L1, and 100 m at L2, L3, and L4, respectively. F_{Ref} is calculated from the intercept. It should be noted that Martin b factors are independent of the reference depth chosen. Highly variable fluxes were observed at L1, consistent with the temporarily variable contributions of anchovy fecal pellets and with satellite imagery (Appendix A, Fig. A1-1). At L2, flux increases with depth. Strongly reduced fluxes were observed in the transitional waters of L3 while L4 had fluxes as high as observed at L1.

Figure 16 (a and d) shows grand averaged attenuation flux profiles for 30-100 µm, 100-200 µm, 200-400 µm, 400-1000 µm, >1000 µm, and total flux at the 4 locations. Shown also are data from Martin/Knauer style sediment traps deployed to 150 m which were drogued at 15 m (Kranz et al., 2020). Figure 16 (b and e) shows Attenuance flux for the 5 size categories expressed as a fraction of total flux and Fig. 16 (c and f) shows number flux profiles. Martin curve fits to attenuation and number fluxes are tabulated in Tables 2 and 3.

At L1, export was high with a diverse assemblage of material, driven by large aggregates and anchovy fecal pellets. Previous research has found that these large and dense fecal pellets are very efficient transporters of organic matter from the surface ocean into the deep ocean. (Saba and Steinberg, 2012). SEM imagery of CFE-Cal samples revealed that the anchovies were primarily grazing on diatoms. Another indication of the efficiency of transport comes from the analysis of phosphorus and organic carbon in CFE-Cal samples. Phosphorus is known to be lost rapidly relative to organic carbon from sinking particles (Collier and Edmond, 1984); Anchovy pellet dominated samples collected using the CFE-Cal at L1 had an organic carbon to phosphorus (C:P) ratio of 60:1, much lower than typical 300:1 ratio found in other samples (Bourne et al., 2019). Though greater than 90% of the particle number flux at 125 m at L1 was in sizes less than 200 µm in diameter, particles greater than 1000 µm in size carried 90% of particle flux (Fig. 16).



At location L2, the flux at 150 m was dominated by 200-400 μm sized olive colored ovoid fecal pellets. Number fluxes were 150,000 $\text{m}^{-2} \text{d}^{-1}$. Evidence suggesting a fast sinking rate for these particles was that they accumulated at the edges of the sample stage reflecting the focusing effect of the tapered funnel (Fig. 14, L2 at 150m); aggregates were more evenly distributed across the sample stage. At this depth, $>1000 \mu\text{m}$ aggregates accounted for less than 0.5% of particle number flux but $\sim 40\%$ of attenuation flux. In deep waters aggregates accounted for 95% of the flux. At L3, flux was lower overall but $> 1000 \mu\text{m}$ sized aggregates carried $\sim 70\%$ of attenuation flux at 150 m, with aggregate contribution increasing to 80% in deeper waters. At L4 $>1000 \mu\text{m}$ sized aggregates carried about 85% of the particle flux at 150 m, increasing to $>90\%$ in deeper waters (Fig. 16b).

We apply the Bourne et al. (2019) factor of 0.97 to convert attenuation flux ($\text{mATN-cm}^2 \text{cm}^{-2} \text{d}^{-1}$) to POC flux in ($\text{mmol C m}^{-2} \text{d}^{-1}$). POC flux at 150 m at L2, averaged 12.4 $\text{mmol C m}^{-2} \text{d}^{-1}$ and ranged from 5.0-30 $\text{mmol C m}^{-2} \text{d}^{-1}$. (Fig. 16). Flux through 150 m L3 was the lowest of any location, with an average of 3.0 $\text{mmol C m}^{-2} \text{d}^{-1}$, and ranged from 1.1-5.9 $\text{mmol C m}^{-2} \text{d}^{-1}$. Though surface nitrate was relatively low at L4, flux at 150 m was relatively high and averaged 25 $\text{mmol C m}^{-2} \text{d}^{-1}$ (ranged from 5 to 72 $\text{mmol C m}^{-2} \text{d}^{-1}$).

Interestingly, none of the locations showed a strong decrease of flux with depth as one would expect based of the traditional Martin curve (Fig. 16). Fluxes at L1 and L2 show little change or increase with depth while at L3 and L4, fluxes decrease slowly with depth with 'b' factors -0.4 and -0.3 , trends similar to those reported by Bishop et al. (2016).

Total POC Flux increased with depth at L2 (Fig. 16). Flux at 150 m averaged 12.4 $\text{mmol C m}^{-2} \text{d}^{-1}$. By 250 m, flux had more than doubled to 28.3 $\text{mmol C m}^{-2} \text{d}^{-1}$; by 500 m flux had tripled to 38 $\text{mmol C m}^{-2} \text{d}^{-1}$ (Fig. 16). The data was fit with a Martin $b = +0.87$. The fit for attenuation flux carried by $>1000 \mu\text{m}$ aggregates yielded $b = +1.44$; fit for 200-400 μm flux yielded a $b = -1.71$. The 30-100 and 100-200 μm classes also followed decreasing trends with b factors of -0.63 and -0.71 , respectively. Fits using the fast method (Sect. 2.2.3) yielded pellet and aggregate b factors of -1.07 and $+1.34$, respectively (Bourne, 2018).

At L3, in transitional waters outside the filament, flux slowly decreased with depth. VAF at 150 m (about 100m below the euphotic zone) was 3.8 $\text{mmol C m}^{-2} \text{d}^{-1}$. At 250 m and 500 m, fluxes were 3.9, and 2.4 $\text{mmol C m}^{-2} \text{d}^{-1}$, respectively.

3.4 Water Column POC

Transmissometers, which measure beam attenuation, can be used to quantitatively estimate POC in the water column (Bishop, 1999; Bishop and Wood, 2008). Beam attenuation is strongly correlated to POC in the upper kilometer of the water column. Between 41 and 89% of this signal is typically due to beam interaction with relatively small, slowly-sinking particles (Chung et al., 1996; Bishop, 1999). Surface layer transmissometer-derived POC ranged from a high of 35 μM at L1, to a low of 2 μM at L4 (Fig. 10).

The integrated standing stock of POC in the water column was highest nearest shore at L1 and progressively dropped with distance off shore (and time) in the filament (Fig. 10). At L1, where the sea floor was at 450 m, relatively high POC levels



(averaging $\sim 1 \mu\text{M}$) were detected in the 300m to 450 m interval, indicative of resuspended particles forming a bottom nepheloid layer.

3.5 Surface Export

420 Euphotic zone new production (NP) measurements at locations L1, L2, L3 and L4 (converted to carbon units) were 189 ± 21 ,
156 \pm 77, 63 \pm 33, and 19 \pm 3 $\text{mmol C m}^{-2} \text{d}^{-1}$, respectively (Kranz et al., 2020). In this study, CFEs were programmed to dive
no shallower than 100m and fluxes were lower than NP values at all locations except at L4, the last occupation of the filament,
where POC flux measured by CFEs exceeded NP by a factor of >2 at 250 m. In this case, we use nitrate and beam attenuation
coefficient (POC) to estimate shallow export for the time interval spanning the occupations of L2 and L4. We have confidence
425 in this calculation since a sediment trap array, drogued at 15 m, deployed late in the study at L2 tracked the water to L4 (Kranz
et al., 2020); furthermore, L2b and L4 salinity profiles were virtually identical (Fig. 12), thus indicating that the water masses
encountered in the later part of occupation at L2 were of similar origin to the water mass encountered at L4. Thus the 4.6 μM
nitrate draw down of nitrate in the upper layer (Fig. 12) reflects biologically mediated uptake of nitrate and particle export.

Following Johnson et al. (2017), we calculate export by integrating nitrate drawdown from surface waters and then convert to
430 carbon using a ratio of organic carbon to nitrogen. Johnson et al. (2017) used a Redfield ratio of 6.6 C/N; we used a C/N of
6.4 (Stukel et al., 2013) for our calculation. An integration depth of 45 m was chosen as dissolved nitrate levels from the two
sites converge at this depth (Fig. 12) and also because 45 m was close to the euphotic zone depth at L4. Subtracting integrated
nitrate at L4 from L2b and scaling by C/N ratio yields an average new production of 111.3 ± 32.2 (S.D.) $\text{mmol C m}^{-2} \text{d}^{-1}$ over
9 days, similar to NP measured at L2 but a factor of 6 higher than reported at L4 by Kranz et al. (2020).

435 Integrating POC stocks measured using the transmissometer from the surface to 45 meters at L2b and L4 allows us to estimate
the average rate of loss for POC of $33 \text{mmol C m}^{-2} \text{d}^{-1}$. Combined, NP and POC losses allow calculation of how much material
was exported from the euphotic zone.

4. Discussion

4.1 Circulation

440 When considering carbon export dynamics, especially in regions with strong current systems, it is essential to understand the
vertical profile in the context of the physical environment. As mentioned previously, by June 20–25, a depression in sea surface
height (SSH) roughly 100 km in diameter had developed about 200 km off the coast. Such a SSH depression indicates the
formation of a cyclonic eddy as Ekman transport would yield a net transport out of the center to the edge of the eddy as waters
rotate clockwise around the center. As CFEs are Lagrangian, they drift with currents at depth during deployments, and their
445 positions over time can be used to infer current velocity. The CFE trajectories of dives deployed from 150 to 250 m all reinforce



such counterclockwise motion, consistent with ADCP data (Fig. 4). Water on the shelf at L1 was affected by tidal motion but overall flowed offshore to the west. By L2, the water was flowing quickly to the west-north-west. As this westward flowing water encountered offshore water flowing eastward, a cyclonic eddy formed, with anticyclonic eddies forming to the north and south. L3 was located outside of a developing cyclonic eddy, with water moving quickly to the south east. L4 was in slow moving waters close to the center of the eddy. These large-scale circulation patterns, with consistent directionality of water flow encountered by CFEs at all depths has implications for the flux profiles as discussed in depth below.

4.2 Comparison with other studies

Siegel et al. (2014) estimated algal aggregates and zooplankton fecal matter export at the base of the euphotic zone from a food web model driven by satellite observations including SST, chlorophyll a concentration, net primary productivity and particle size spectrums for monthly climatological conditions. The Siegel et al. (2014) climatological flux for June in our region is shown in Fig. 15. Recognizing the spatial coarseness of Siegel et al.'s 1x1 degree gridded data set, the model predicts a base of euphotic zone flux of about $20 \text{ mmol C m}^{-2} \text{ d}^{-1}$ near-shore with progressively lower fluxes further off shore to about $5 \text{ mmol C m}^{-2} \text{ d}^{-1}$ at offshore L3. In order to compare CFE flux results at 150 m and 250 m, these modeled euphotic zone export magnitudes were extrapolated to 150 and 250 m using Eqn. (1), and a b value of -0.83 from the Martin et al. (1987) VERTEX1 site (Fig. 2). In all cases our observed fluxes are higher. The point of this comparison is that filaments make a disproportionately large contribution to carbon transfer to deeper waters and that such filaments need to be included in models. Deutsch et al. (2020) describe new eddy resolving simulations of biogeochemical processes in the California Current regime which can be informed by the work described here.

One of the closest observations in terms of distance from coast, season, and span of the water column is the VERTEX-1 (V1) reported in the classic Martin et al. (1987) study. Martin's station V-1, occupied in June 1984 in intense upwelling and high chlorophyll conditions, was located off the coast of Point Sur at the same longitude as L2 but approximately one-degree further north (Fig. 2). VERTEX deployed surface tethered particle interceptor (PIT) sediment traps from 50 to 2000 m. V-1 fluxes at 50 and 100 m, were 25 and $19.6 \text{ mmol C m}^{-2} \text{ d}^{-1}$. At L1, our CFE fluxes at 50 m and 125 m, were 21 and $50 \text{ mmol C m}^{-2} \text{ d}^{-1}$, respectively. Although V-1, fluxes were similar to our results, the profiles in deeper waters diverged. Flux at L1 was nearly constant or slowly increasing with depth; and the flux at L2 increased with depth; in contrast, V-1 data decreased strongly following the power law function (Eqn. 1) with a b value of -0.83.

The comparison with VERTEX results is justified since Point Sur has been identified as an area of frequent filament development (Abbot and Barksdale, 1991; Gangopadhyay et al., 2011); furthermore, chlorophyll fields mapped using the NASA Coastal Zone Color Scanner in June 1984, although few, confirm a filament structure near V-1 at the time of sampling. There are two candidate explanations for why VERTEX V-1 results and our data taken in similar conditions display such different behaviors. First, L1 was located over a wide 500 m deep "shelf" and L2 offshore was down current of this feature,



whereas V-1, in 3 km deep water, was offshore of a much narrower shelf (Fig. 1). When high export occurs over a broad shelf, particles can accumulate in a fluff layer near bottom and resuspended in a nepheloid layer. Such a layer can clearly be seen at L1 in both transmissometer derived POC and in water turbidity (Fig. 10) and thus there is a potential source of particles to offshore waters.

The second possible explanation is that many of the $>1000 \mu\text{m}$ sized aggregates seen in CFE imagery would be excluded from surface tethered baffled PIT traps due to ‘baffle bounce’, observed when currents relative to the trap are faster than 0.02 m s^{-1} (Bishop et al., 2016). Stated another way, the size scale of the aggregates relative to the cm-scale baffle opening on traps, coupled with a near horizontal encounter with the trap opening would cause aggregates to bounce back into the flow and thus not be sampled. This was observed using surface-tethered OSR instruments during quiescent conditions in the Santa Cruz Basin. In our observations, currents were generally faster than this threshold. While smaller particles at L2 did attenuate with depth, aggregate fluxes increased (Fig. 16), thus there is support for this hypothesis.

Surface-tethered traps identical to Martin et al. (1987) were deployed at 50,100, and 150 m during the CCE-LTER study (Kranz, et al. 2020). At 150 m at L1, L2 and L4, trap measured flux and CFE derived fluxes (Fig. 16) were in close agreement. At L3 in transitional waters, PIT trap fluxes at 150 m were two times higher than CFE results; however, the strong surface current regime encountered there rapidly separated the two observing systems spatially. Based on the reasonable agreement of results, the second candidate explanation is disfavored.

A question may be asked, “If trap fluxes from 50, 100, 150 are fit with a Martin fluctuation, does the extrapolated curve adequately match fluxes observed by the CFEs deeper in the water column”? Figure 16 depicts PIT fluxes extrapolated to depth using the best fit b factor for the 50-150 m results. At L1, L2, L4, and L3 Martin b values were -0.31, -0.85, -0.31, and -2.12, respectively. At 300 m (L1) and 500 m at L2 and L3, Martin-extrapolated fluxes were lower than CFE fluxes by factors of 2.1, 6.8, and 4.9. Only at L4 did fluxes agree well. The first take away is that Martin b factors are rarely ‘Classic’ and often are substantially lower than expected. The second, take away is that the mismatch (Martin vs. CFE) indicates that fundamental processes contributing to the flux profile are not accounted for by the Martin relationship in deeper waters.

Considering the two candidate explanations above, we hypothesize that proximity to a wide-shallow continental margin environment leads to more efficient transfer of POC through the water column. More work on the intercomparison of PIT traps and CFEs, particularly particle classes sampled, would resolve any sampling bias issues. While mesoscale (4km) chlorophyll variability (Sect. 3.2; Fig. 5) at L2 is small, there is no insight regarding the variability of particle flux. Clearly, future experiments in dynamic filaments will benefit from expanded deployment autonomous flux measuring systems.

4.3 Mechanisms for Non-Classic Martin Behavior

In the CCE_LTER process study reported here, we do not observe flux attenuating significantly with depth deeper than 100 m at any of our locations. At two locations we see flux near constant or increasing with depth. At other locations we observe



cases where flux decreases with depth at a rate far less than predicted by the Martin formulation. We explore reasons why the flux profile from the coastal station VERTEX1 (Martin et al., 1989, Fig. 1), which follows the classic curve, differs from results of this study. In the following discussion, we use the term “non-classic” to represent such behavior.

Caveat on the assumed constancy of the CFE ATN:POC calibration factor with depth. Calibration studies, described in Bourne et al. (2019) were restricted to deployment of sample collecting CFE-Cals near 150 m for ship time logistical reasons, the need for replication, and for comparison with PIT trap data; for these reasons we do not have calibration samples for samples taken at 250 m and 500 m. We do not believe that this is a limitation because samples collected at 150 m covered a wide range of size distribution and particle types; furthermore, Estapa et al. (2017) did calibrate POC vs. attenuation flux at different depth intervals and found that all samples plotted on the same slope suggesting little depth dependence of calibration. We add to this the observation that, large particles sampled by in-situ filtration show little shift in organic carbon percentages from the base of the euphotic zone to 500 m (e.g., Bishop et al., 1986). In the future, CFE-Cals will be deployed to at least 500 m to validate the POC:ATN relationship as a function of depth. A caveat for the following discussion is that the Attenuance:POC flux relationship and its assumed constancy with depth is not a factor in the interpretations that follow.

Figure 18 depicts four mechanisms which could explain why particle flux profiles may diverge from traditional Martin-like behavior: (1) non-steady state flux and/or remineralization; (2) inputs from migratory organisms at depth; (3) physical subduction of surface material along isopycnal surfaces; (4) lateral horizontal transport of resuspended particles from the continental margin.

4.3.1 (M1) Non-Steady State Flux

The Martin et al. (1987) formula assumes constant export and remineralization over the time scale required for particles to transit from the base of the euphotic zone to 500 m, typically in 4-5 days; however, CCE-LTER sampled a rapidly evolving system. Upwelled coastal water can spawn productive filaments and eddies that persist shorter than a month. Giering et al. (2016) describe cases, especially associated with bloom scenarios, where the water column may not be in steady state. Figure 19 depicts two such scenarios in which export and remineralization are time varying in a way that leads to an apparent non-varying flux with depth or to an increased flux with depth.

Non-steady state blooms and time variable changes of b factor can lead to inverted Martin curves as there is a temporal lag between peak biomass at the surface and peak flux to depth as particles take time to settle (Figs. 18a and 19). One indicator of temporal delay would be slowly sinking ungrazed intact phytoplankton from the remains of a bloom seen at depth. CTD Chlorophyll fluorescence data, however, shows no evidence of sinking ungrazed phytoplankton (Figs. 10 and 11). Furthermore, there is also no significant trend of flux either increasing or decreasing with time particularly at L2 (Fig. 5). That particle flux at L4 was 2.5 times higher than measured new production provides some support for the non-steady state flux mechanism.



4.3.2 (M2) Efficiency of Grazing Community and Active Transport

540 Zooplankton are highly important to POC export as their fecal pellets or feeding webs package smaller non-sinking phytoplankton and particles; however, flux due to zooplankton produced fecal pellets and aggregates is highly dependent upon the zooplankton community present (Turner, 2015; Bishop et al., 1986; Boyd et al., 2019). Furthermore, the community of phytoplankton that develop seasonally and during the course of a bloom can have great impact on how surface material is exported to the mesopelagic.

545 High levels of production and biomass do not necessarily imply high export (Bishop et al., 2004, 2016; Lam and Bishop, 2007). In a multi-cruise study in the Santa Cruz Basin south of the CCE-LTER study area, Bishop et al. (2016) found that highest export levels coincided with lowest levels of surface chlorophyll. None of the flux profiles from the cruises (January, March and May) were traditional Martin curves (Fig. 1). High levels of productivity, combined with efficient grazing and weak remineralization likely combined to create the conditions of very high flux observed in January 2013 (Bishop et al., 2016).

550 Vertical migrators can also transport material to depth (Fig. 18b). Diel vertical migrators such as euphausiids, salps and copepods consume material at the surface during feeding times, and then can excrete material when they retreat to depth (Steinberg et al., 2008). Fish can also transport consumed material to depths below the euphotic zone.

555 Some heterotrophs produce fecal material that is much more efficient at being exported from the euphotic zone. Organisms such as krill and fish produce large dense fecal pellets which sink very efficiently. At L1, the near constant flux with depth was due in large part to anchovy pellets sinking quickly. Saba and Steinburg (2012) found that similarly sized anchovy pellets sank on average faster than 750 m d^{-1} . It has been reported that both copepod (Smetacek, 1980; Krause, 1981; Bishop et al., 1986; Bathmann et al., 1987; Gonzalez et al., 2000) and protozoan (Gonzalez, 1992b; Beaumont et al., 2002) pellets do not have high transfer efficiency on sinking from the euphotic zone. Gonzalez (2000) found only 0.1-2.5% of copepod fecal pellets in the upper 100m Humboldt current reached sediment traps at 300m. The fast recycling of ovoid copepod fecal pellets in the surface has been attributed primarily to coprophagy, the process by which zooplankton eat other zooplankton's feces (Beaumont et al., 2002; Smetacek, 1980). Evidence suggests that the fast recycling of zooplankton pellets in the epipelagic is due to the activities of other zooplankton (Turner, 2015 and references therein). There are a number of zooplankton known to eat feces (coprophagy) including radiolarians (Gowing et al., 1989), tunicates (Pomeroy et al., 1984) and copepods (Sasaki et al., 1988).

565 At L2 at 150 m, 200-400 μm sized ovoid pellets were very abundant and were obviously fast sinking. At 100 and 150 m, the ovoid pellet number flux was $150,000 \text{ m}^{-2} \text{ d}^{-1}$. However, by 250 m, the pellets flux was reduced by a factor of 7 and by a total factor of 20 to 500 m (Fig. 8a), These trends were confirmed and calibrated by manual particle counts (Connors et al., 2018). The membrane-bound small ovoid pellets were olive colored (Fig. 6g) and shown in SEM imagery to be full of diatom frustules



and fragments. We also note that pellet flux decrease was a universal feature at all locations; at L3 and L4 from 100 to 500 m, the decreases were by factors of 6 and 4, respectively; at L1 the decrease was 2.5-fold between 50 and 250 m (Fig. 8c).

At L2, as the ovoid pellets decreased with depth, the concentration of aggregates, many of which closely resemble discarded larvacean houses, began to dominate export (Fig. 16). Larvaceans produce fine mucous feeding webs that concentrate and ingest particles from 0.2 to 30 μm in diameter (Gorsky and Fenaux, 1998). Typically, a larvacean feeds on only a fraction of the material in their web before it discards it due to clogging (Berline et al., 2011). Some larvaceans create and discard up to 26 feeding webs a day. They therefore can be major contributors to carbon flux. Larvaceans can be found throughout the upper 1000 m (Stemmann et al., 2008) and they are often the most abundant mesozooplankton after copepods (Gorsky and Fenaux, 1998). In many food web models, the mesozooplankton component typically lumps all mesozooplankton together and is more parameterized towards representing copepods (Berline et al., 2011). Larvaceans with intact feeding structures are difficult to study as they are fragile, and therefore difficult to capture in either plankton nets as they are prone to break (Berline et al., 2011; Silver et al., 1998). The larvaceans are captured in net tows; however, newly reported results from *Zooglider*, an autonomous buoyancy driven glider with interfaced zooplankton imaging system, showed order-of-magnitude higher abundances of larvaceans compared simultaneous MOCNESS collections during operations in the vicinity of the La Jolla canyon in March 2019 (Whitmore, et al., 2019). The full extent of actions of migratory communities and their modification of sinking particle flux is, at yet, only partly realized.

Vertical migration likely does contribute export to depth. At L2, we did see evidence of migration to 250 m in preliminary biomass profiles from MOCNESS tows (Ohman, personal communication, July 2020) and in ADCP scattering intensity records. However, the increase of flux with depth cannot solely be explained through transport of material from the surface to depth through vertical migration. For one, vertically migrating crustacean species in the CCE have a gut turn over time of about 30 minutes, thus in 1-2 hours to swim to depth and only 50% or 25% of excreted material would be delivered to 250 m, where we see increased flux. The aggregates at depth are clearly not aggregations of fecal pellets. This does not rule out that vertical migrators were important, as gelatinous organisms such as larvaceans and salps have been known to migrate daily. A quantitative analysis of the CCE-LTER MOCNESS speciation and of multifrequency fisheries echo sounder data would help resolve these questions but has yet to be performed.

Does active transport explain the flux increase at L2? At L2, Kranz et al. (2020) report a measured new production of $101.6 \pm 44.0 \text{ mmol C m}^{-2} \text{ d}^{-1}$. In close agreement with our calculated new production averaging 111.3 ± 32.2 (S.D.) $\text{mmol C m}^{-2} \text{ d}^{-1}$ using the change of 0-45 m nitrate inventory from L2b to L4 over the 9-day period between studies.

POC inventory changes between the two times gives us a further net loss of $33 \text{ mmol C m}^{-2} \text{ d}^{-1}$. Typically, crustacean grazers assimilate about 70% of food consumed, passing on 30% of material as fecal pellets, thus, sinking products from the POC loss would only add $\sim 10 \text{ mmol C m}^{-2} \text{ d}^{-1}$ sinking below 45 m. This added to new-production gives a total export of $120 \text{ mmol C m}^{-2} \text{ d}^{-1}$.



These sinking particles are consumed by particle grazers and assimilation efficiency can vary by species and food substrate. Previous work has reported that salps have a 61% assimilation efficiency for carbon (Madin and Purcell, 1992). If exported particles were processed using this efficiency, and if all particles were consumed by vertically migrating organisms and excreted at depth, there would be a flux of 48 mmol C m⁻² d⁻¹. The same calculation assuming an assimilation efficiency of 90%, would add ~12 mmol C m⁻² d⁻¹ at depth. Flux at 500 m at L2 was 38 mmol C m⁻² d⁻¹ which would require dominant migratory inputs. Therefore, while the community of grazers present, and vertical migrators, are likely important contributors to flux, their activities may not fully explain the depth increasing flux profiles observed at L2. It is clear that the flux carried by aggregates at depth cannot form from the coprophagy of sinking fecal pellets.

4.3.3 (M3) Physical Subduction

Particles are transported by both gravitational sinking and currents. When currents transport euphotic zone particles by subduction along isopycnal surfaces this adds to carbon export (Fig. 18c). In most regimes, export of particulate organic carbon (POC) to depth is primarily attributed to sinking particles; however, in dynamic regimes sub-mesoscale eddy driven flux may be responsible for delivering a significant percentage of POC along isopycnal surfaces to depth (Omand et al., 2015). There is no evidence to support a subduction contribution as explanation of the flux increases with depth seen in our CFEs at L2. Isopycnals were mostly horizontal at L1, L2 and L4. Chlorophyll fluorescence profiles (Fig. 10) show minimal penetration of material deeper than 100 m. Spatial transects across the filament furthermore showed little evidence of particles deeper than the 100 m deep 26.0 σ_θ surface (Fig. 11).

Eddy features can play an important role in the subduction of particles. Anticyclonic eddies push water toward the center, forming a dome at the center of which downwelling occurs. Such downwelling would lead to downward transport of particles. However, the filament we followed produced a cyclonic eddy whereby surface water was pushed to the edges, leaving a depression in the middle which would have led to upwelling, not downwelling. Eddy driven subduction therefore did not play a role in fluxes seen in our data.

4.3.4 (M4) Lateral Advection

Deep water currents flowing along continental shelves can pick up sea floor sediments and then transport this material out to sea as it flows along isopycnals (Fig. 19d). Once offshore, filter feeding organisms can consume the particles and produce sinking material adding to vertical flux measured by CFEs or capture by sediment traps. In the eastern boundary current of the North Pacific, lateral transport has been found to play an important role in a number of processes. Intermediate nepheloid layers found several hundred meters below the surface off the coast of Oregon were likely to be the product of lateral advection resuspended particles from the continental shelf (Pak et al., 1980). Intermediate nepheloid layers have also been observed forming between 70 and 150 m depth on the outer shelf of the northern California continental margin (McPhee-Shaw et al., 2004). In a box model study, Alonso-Gonzalez et al. (2009) estimated suspended POC lateral transport in the Canary Current



region to be up to 3 orders of magnitude higher than vertical fluxes, carrying material up to 1,000 km offshore. Their results suggest that laterally suspended POC advected from the continental shelf could be a significant part of the mesopelagic carbon current budget in the Canary Current and that if this is true in other boundary regions, this transport may play a crucial role in
635 global carbon cycle.

Kelly et al. (2018) found an inverse relationship with higher e-ratios (export at euphotic zone base/net primary productivity) in offshore regions and lower e-ratios in the more productive coastal regions over 5 CCE cruises. Furthermore, a strong correlation between sea surface temperature and export was found, which they determined not to be causal, but rather an effect of lateral advection bringing upwelled, cold productive waters offshore.

640 Observed nepheloid layers near L1 might indicate that lateral transport could be a possible factor explaining flux increase with depth at L2 in our study. Support for this comes from the finding of strong currents moving westward off the coast between the surface and 400m during the time of our deployments at L2 (Fig. 8B and 8C). During the first two days of the CFE deployment, these currents moved rapidly to the northwest, with velocities averaging 0.2 m/s between 100 and 300 m. Although, the narrow band 150 kHz ADCP data only resolved current velocity components to about 350 m, CFE trajectories
645 during 500 m dives indicate that deeper water was also moving in the same direction (Fig. 8). The offshore flowing currents, coupled with a high concentration of non-sinking POC over the shallow continental margin at L1 could lead to slow-sinking material being transported offshore to form a substrate for particle grazers.

L2a was only about 50 km from L1 and ~30 km from the 500 m bathymetric contour. Though we did not measure sinking speeds of aggregates, the sinking rates for similarly sized aggregates and discarded larvacean houses measured in Henson et al. (1996) was 120 m d⁻¹. Calculations for particles sinking at 100 m/day (Sect. 3.2) suggests a lateral displacement of between
650 15 and 30 km. It is possible that aggregates from L1 could be transported offshore, explaining the apparent increase of flux with depth observed at L2.

Several points of evidence argue against this. First, the high POC layer at L1 seen between 300-450 m (Fig. 10) occurs in waters denser than the $\sigma_{\theta}=26.7$ isopycnal, while a subsurface POC feature is seen at L2a, it is present in much shallower less
655 dense waters; the feature is absent at L2b. This disconnect of L1 and L2 is more readily seen in Fig. 11 which contours POC against potential density. UVP5-hd data shows that the nepheloid layer at L1 is dominated by smaller particles and not >1000 μm sized aggregates. In fact, in the 100-300 m depth interval there were fewer >1000 μm aggregates at L1 than at L2, and aggregates had identical concentrations below 300 m (Fig. 20). This rules out a direct connection involving the advection of large aggregates or resuspended small particles from L1.

660 While it seems likely that both active transport (M2) and perhaps a 3D lateral advection effect (M4) may play a role in the flux profiles observed, more work is necessary to understand each mechanisms' contribution. Non-steady export (M1) may have been a factor at L4. The 3D nature of particle entrainment and lateral transport of water forming the plume needs to be explored.



4.3.5 Other factors. Continental Shelf Width.

Reducing continental shelf sediments have been documented to be important sources for the supply of bioavailable iron to surface water phytoplankton communities (Johnson et al., 1999, Chase et al., 2007, Lam et al. 2008). Chase et al. (2007) found that continental shelf width plays an important role in iron availability with narrow continental shelf regimes being more iron limited. We use the analogy to iron supply to raise the question of whether flux profile differences seen during VERTEX 1 vs. the CCE-LTER study are a consequence of shelf width. In other words, is there an intrinsic difference in the zooplankton community composition, grazing and migratory behavior (M2) in slope waters near narrow vs. wide continental shelves?

670 5. Conclusions

Coastal upwelling regions are disproportionately productive relative to their total surface area due to high levels of available nutrients. Four Lagrangian Carbon Flux Explorers (CFE) were deployed a total of two dozen times during the June 2 through July 1 2017 California Current Ecosystem – LTER process study of a dynamic filament of productive water as it moved from the coast to the open ocean.

675 The CFEs provided an unparalleled view of particle flux and particle flux size distribution (30 μm to cm scale) within that system. In all environments, flux was dominated by particles $>200 \mu\text{m}$ in size. At L1, $>1000 \mu\text{m}$ anchovy pellets dominated. At L2, 200-400 μm sized olive colored ovoid pellets contributed on average $\sim 50\%$ of the flux and at times accounted for 100% of the flux at 100 to 150 m. At all locations, $>1000 \mu\text{m}$ sized amorphous aggregates dominated flux at depths greater than 150 m.

680 We found during the CCE-LTER study that flux does not decrease with depth following a typical Martin power law ($b = -0.83$) relationship. Extrapolating POC flux from the euphotic zone to depth using the classic Martin curve in such productive regions strongly underestimates flux. CFE derived Martin ‘b’ factors for flux were +0.1, +0.9, -0.4, and -0.3 at locations L1 through L4, respectively. The most negative b factor was found in the transitional waters just outside of the filament. Interestingly, flux profiles for particle classes smaller than 400 μm , always had negative b factors which were more closely in agreement with
685 the classic Martin fit.

In this study of particle fluxes from 100 m to 500 m, the highest flux was found at L1, where surface chlorophyll initially exceeded $>10 \text{ mg m}^{-3}$. However, the magnitude of flux did not always correlate with surface chlorophyll. L4 had nearly the same flux, though surface chlorophyll was 50 times lower than at L1. We confirm the Bishop et al. (2016) conclusion that surface chlorophyll in the California coastal environment is a poor indicator of flux at depth. The efficiency of export was clearly affected by trophic structure. At L1, flux was very efficient as anchovies directly grazed on primary producers, and produced dense phosphorus-rich, fast sinking pellets. At L2, though copepods were ubiquitous higher in the water column and their fecal pellets an important contributor to flux at 150 m, the contribution had largely disappeared by 250 m depth. At all
690 locations the ovoid fecal pellet fluxes decreased as expected with increasing depth (Fig. 8) consistent with their production in



695 or just below the euphotic zone and progressive loss with depth. Their pellets were therefore not significant contributors to carbon flux deeper in the mesopelagic.

At both L2, and to some extent at L1, there was a shift from fecal pellets near the surface to large aggregates at depth. At L3 and L4, large aggregates were present at all depths. These aggregates resembled discarded larvacean feeding webs. There was some evidence that westward moving currents laterally transported waters with POC from the continental shelf, although a direct connection between L1 and L2 could not be established.

700 The flux profiles observed at all locations were unlike the classic Martin curve. As mentioned previously, the VERTEX-1 site in the classic Martin et al. (1987) study was located 100 km north of our L1 and L2 study areas and took place under similar conditions (including active upwelling and the presence of a filament). The reason for the differing vertical profiles of the VERTEX 1 site compared with our L1 and L2 may be related to the width of the continental shelf/marginal basins – most likely structural ecosystem differences – at the two different sites.

705 At this writing, we find the data are insufficient to explain the particle flux increase at L2 between 100 and 500 m, and we have not closed the story of the origins of the aggregates that dominate flux in all waters deeper than 150 m. This study shows that there are many new questions pertaining to filament dynamics and POC flux.

Fluxes made with surface-drogued PIT traps were generally in agreement with CFE fluxes near 100 and 150 m, suggesting that discrimination against $>1500 \mu\text{m}$ aggregates as proposed by Bishop et al. (2016) may not be as important in the strong
710 upwelling and wave conditions encountered during the CCE-LTER study. Extrapolation of 50-150 m PIT fluxes to depth using Martin fits, led to significant (factors of 3 to 7) underestimation of flux at the deepest depth horizon sampled by CFEs again raising the question of how the deep aggregate populations and fluxes are achieved.

Unlike, sample collecting devices (including CTD/rosettes, drifters, surface drogued sediment traps, and CFE-Cals) that must be ship-deployed, CFEs have a mission capability of 8 months of hourly operations (16 months 2 hours ...) and have been
715 deployed for missions up to 40 days without compromise; the CFEs have been proven in a wide range of sea states and to depths of 1000 m (Bishop et al., 2016). Due to the complexities of particle size distribution and particle class measurement, which is not yet implemented on the CFE, all deployments have been tended by ships to date. The framework provided by the CCE-LTER process study provided an opportunity to advance towards full CFE autonomy while supporting science. Our hybrid size distribution analysis scheme provided key insights that are an important step towards fully autonomous operations
720 in the global ocean.

In coastal regions, carbon export needs to be understood both laterally and vertically. A future expanded scope of autonomous observations during process studies and surveys would provide a 3D view of mechanisms dictating export in these regions and inform the new class of eddy resolving simulations of biogeochemical processes in the California Current System such as recently described by Deutsch et al. (2020).



725 **Data Availability.** Carbon Flux Explorer original transmitted light imagery and derived attenuation imagery (~1600 images each) and tabular size-analysis results from these images is archived at the Biological and Chemical Oceanography Data Management Office at Woods Hole Oceanographic Institution (Bishop, 2020a; Bishop, 2020b). The sources of all other data are identified in the text.

730 **Author Contributions.** HLB as part of her Ph.D. dissertation, played lead role in precruise laboratory preparation and CFE system assembly and testing; at sea HLB was science lead on deployment and recovery of CFEs; post cruise HLB led laboratory analysis of samples; she developed fast algorithms capable of running on the CFE in real time and codes that provided physical and hydrographic context for our observations; she developed the interpretive template for this manuscript. JKBB served as advisor to HLB during her Ph.D. dissertation and was PI of the project; at sea he maintained CTD-deployed particle concentration sensors and performed all CTD particle optics data reduction, he served as a third hand during CFE
735 deployments and recoveries; postcruise he developed the hybrid particle size analysis codes, and analysed remote sensing data sets. He led the preparation of this manuscript for publication. TJW was lead on all engineering activities for CFE systems and their precruise ballasting; at sea, he maintained the CFEs and closely worked with HLB on CFE deployments, operations, and recoveries. ELC performed size distribution analysis of aggregates and pellets used to validate the refinement of a pellet classification scheme developed by JKBB.

740 **Acknowledgements.** We would like to thank Mark Ohman (chief scientist), Mike Stukel (USF), members of the science party, and the captain and crew of the R/V Revelle for support during the 2017 CCE-LTER process study. Tim-Lowe (LBNL, Engineering – design lead) and Lee-Huang Chen (UC Berkeley, Engineering) contributed substantially to project success. We thank Mark Ohman for inviting us to sea and Mike Stukel for feedback and discussion of this manuscript. We also thank Alejandro Morales (LBNL) and Mike McLune (SIO – Instrument development group). Many UC Berkeley undergraduates
745 aided in CFE related activities at sea and in the laboratory, in particular we thank Casey Fritz, Xiao Fu, Sylvia Targ, Jessica Kendall-Bar and William Kumler. US National Science Foundation grants OCE 1538696 and OCE 1724495 supported development of both CFE and CFE-Cal systems, HLBs thesis research, and seagoing activities. CCE-LTER project (including shiptime) was supported by NSF OCE 1637632.

References

- 750 Abbot, M.R. and Barksdale, B.: Phytoplankton Pigment Patterns and Wind Forcing off Central California. *Journal of Geophysical Research*, 96(C8), 14,649–14,667, doi:10.1029/91JC01207, 1991
- Alonso-González, I. J., Arístegui, J., Vilas, J. C., and Hernández-Guerra, A.: Lateral POC transport and consumption in surface and deep waters of the Canary Current region: A box model study, *Global Biogeochem. Cycles*, 23, GB2007, doi:10.1029/2008GB003185, 2009.



- 755 Bacon, M. P., Cochran, J. K., Hirschberg, D., Hammar, T. R., and Fleer, A. P. (1996). Export flux of carbon at the equator during the eqpac time-series cruises estimated from 234th measurements. *Deep-Sea Research Part II: Topical Studies in Oceanography*, 43(4–6), 1133–1153. doi:10.1016/0967-0645(96)00016-1, 1996.
- Banse, K.: Reflections About Chance in My Career, and on the Top-Down Regulated World. *Annual Review of Marine Science*, 5(1), 1–19. doi:10.1146/annurev-marine-121211-172359, 2013.
- 760 Bathmann, U.V., Noji, T.T., Voss, M., and Peinert R.: Copepod fecal pellet: abundance, sedimentation and content at a permanent station in the Norwegian Sea in May/June 1986. *Mar. Ecol. Prog. Ser.*, 38, 45–51. doi:10.3354/meps038045, 1987.
- Beaumont, K. L., G. V. Nash, and Davidson, A. T.: Ultrastructure, morphology and flux of microzoo- plankton faecal pellets in an east Antarctic fjord, *Mar. Ecol. Prog. Ser.*, 245, 133–148. doi:10.3354/meps245133, 2002.
- Berline, O., Stemmann, L., Lombard, F., and Gorsky, G.: Impact of appendicularians on detritus and export fluxes : a model
765 approach at DyFAMed site, *Journal of Plankton Research*, 33(6), 855–872 doi:10.1093/plankt/fbq163, 2011.
- Bishop, J.K.B.: Regional extremes in particulate matter composition and flux: effects on the chemistry of the ocean interior. In Berger, W.H., Smetacek, V.S., and Wefer, G. eds., *Productivity of the ocean present and past*. Dahlem Konferenzen. Chichester: John Wiley and Sons Ltd.. pp 117–137, 1989
- Bishop, J.K.B.: Transmissometer Measurement of POC. *Deep-Sea Research I*. 46(2) 353-369. doi:10.1016/S0967-
770 0637(98)00069-7, 1999.
- Bishop, J. K.B.: Imagery in attenuation units acquired by autonomous Carbon Flux Explorers deployed 100-500m in the California Current Regime, during the CCE-LTER process study (P1706) between June 2 and July 1, 2017. Biological and Chemical Oceanography Data Management Office (BCO-DMO). (Version 1) Version Date 2020-09-17, 2020a. <http://lod.bco-dmo.org/id/dataset/825076>. doi: 10.26008/1912/bco-dmo.825076.1
- 775 Bishop, J.K.B.: Size fractionated Particulate Carbon Flux 100-500m measured by autonomous Carbon Flux Explorers deployed during the CCE-LTER process study (P1706) between June 2 and July 1, 2017 in the California Current Regime. Biological and Chemical Oceanography Data Management Office (BCO-DMO). (Version 1) Version Date 2020-09-16, 2020a. <https://www.bco-dmo.org/dataset/823408>. doi: 10.26008/1912/bco-dmo.823408.1
- Bishop, J.K.B., Wood, T. J., Davis, R. E., and Sherman, J. T.: Robotic observations of enhanced carbon biomass and export at
780 55 degrees during SOFeX, *Science*, 304(5669), 417–420. doi:10.1126/science.1087717, 2004.
- Bishop, J. K. B., and Wood, T. J.: Particulate matter chemistry and dynamics in the twilightzone at VERTIGO ALOHA and K2 sites. *Deep-Sea Research Part I: Oceanographic Research Papers*, 55(12), 1684–1706. doi:10.1016/j.dsr.2008.07.012, 2008



- Bishop, J. K. B., and Wood, T. J.: Year-round observations of carbon biomass and flux variability in the Southern Ocean. *Global Biogeochemical Cycles*, 23(2), 1–12. doi:10.1029/2008GB003206, 2009.
- 785 Bishop, J. K. B., Fong, M. B., and Wood, T. J.: Robotic observations of high wintertime carbon export in California coastal waters. *Biogeosciences*, 13(10), 3109–3129. doi:10.5194/bg-13-3109-2016, 2016.
- Bourne, H. L.: Marine Biogeochemical Cycling of Carbon and Cadmium. Ph.D. dissertation, University of California, Berkeley, 121 pp., 2018.
- Bourne, H. L., Bishop, J. K. B., Wood, T. J., Loew, T. J., and Liu, Y.: Carbon Flux Explorer optical assessment of C, N and P
790 fluxes, *Biogeosciences*, 16, 1249–1264, doi:10.5194/bg-16-1249-2019, 2019.
- Boyd, P. W., and Trull, T. W.: Understanding the export of biogenic particles in oceanic waters: Is there consensus? *Progress in Oceanography*, 72(4), 276–312. doi:10.1016/j.pocean.2006.10.007, 2007.
- Boyd P. W., Claustre, H., Levy, M., Siegel, D. A. and Weber, T.: Multi-faceted particle pumps drive carbon sequestration in the ocean. *Nature*, 568, 327–335. doi:10.1038/s41586-019-1098-2, 2019.
- 795 Buesseler, K. O., Lamborg, C. H., Boyd, P. W., Lam, P. J., Trull, T. W., Bidigare, R. R., et al.: Revisiting carbon flux through the ocean’s twilight zone, *Science*, 316, 567–571. doi:10.1126/science.1137959, 2007.
- Burd, A. B., Hansell, D. A., Steinberg, D. K., Anderson, T. R., Aristegui, J., Baltar, F., eaurpré, S. R., Buesseler, K. O., DeHairs, F., Jackson, G. A., Kadko, D. C., Koppelman, R., Lampitt, R. S., Nagata, T., Reinthaler, T., Robinson, C., Robison, B. H., Tamburini, C. and Tanaka, T.: Assessing the apparent imbalance between geochemical and biochemical indicators of meso-
800 and bathypelagic biological activity: What the @\$#! is wrong with present calculations of carbon budgets? *Deep Sea Research Part II: Topical Studies in Oceanography*, 57(16), 1557–1571. doi:10.1016/j.dsr2.2010.02.022, 2010.
- Chase, Z., P. G., Strutton, and Hales, B.: Iron links river runoff and shelf width to phytoplankton biomass along the U.S. West Coast, *Geophysical Research Letters*, 316, 567–571, doi:10.1029/2006GL028069, 2007.
- Chung, S.P., Gardner, W.D., Richardson, M.J., Walsh, I.D., and Landry, M.R.: Beam attenuation and micro-organisms: spatial
805 and temporal variations in small particles along 140°W during the 1992 JGOFS EqPac transects. *Deep-Sea Research II*, 43, 1205–1226. doi:10.1016/0967-0645(96)00030-6, 1996.
- Collier, R. and Edmond, J.M.: The trace element geochemistry of marine biogenic particulate matter, *Progress in Oceanography*, 13, 113–199. doi:10.1016/0079-6611(84)90008-9, 1984.
- Connors, E.J., Bourne, H.L., and Bishop J.K.B.: Depth and Temporal Variation of Aggregate Export from the Biological
810 Carbon Pump in Upwelling California Coastal Waters. Presented at the AGU/ASLO Ocean Sciences Meeting, Portland, OR, Feb. 2018. Poster BN14D-1059123, 2018.



- Deutsch, C., Frenzel, H., McWilliams, J. C., Renault, L., Kessouri, F., Howard, E., Liang, J-H., Bianchi, D., and Yang, S.: Biogeochemical variability in the California Current System. *bioRxiv* doi:10.1101/2020.02.10.942565, 2020. (on-line preprint).
- 815 Dunne, J. P., Armstrong, R. A., Gnanadesikan, A., and Sarmiento, J. L.: Empirical and mechanistic models for the particle export ratio. *Global Biogeochemical Cycles*, 19(4). doi:10.1029/2004GB002390, 2005.
- Ebersbach, F., Trull, T.W., Davies, D.M., and Bray, S.G.: Controls on mesopelagic particle fluxes in the Sub-Antarctic and Polar Frontal Zones in the Southern Ocean south of Australia in summer-Perspectives from free-drifting sediment traps. *Deep-Sea Research Part II: Topical Studies in Oceanography*, 58(21–22), 2260–2276. doi:10.1016/j.dsr2.2011.05.025, 2011.
- 820 Eppley, R., Peterson, B.: Particulate organic matter flux and planktonic new production in the deep ocean. *Nature* 282, 677–680. doi:10.1038/282677a0, 1979.
- Estapa, M. L., Siegel, D. A., Buesseler, K. O., Stanley, R. H. R., Lomas, M. W., and Nelson, N. B.: Decoupling of net community and export production on submesoscales in the Sargasso Sea. *Global Biogeochemical Cycles*, 29, 1266–1282. doi:10.1002/2014GB004913, 2015.
- 825 Gangopadhyay, A., Lermusiaux, P.F.J, Rosenfeld, L., Robinson, A.R., Calado, L., Kim, H.S., Leslie, W.G., and Hawley, P.J.: The California Current System: A multiscale overview and the development of a feature-oriented regional modeling system (FORMS). *Dynamics of Atmospheres and Oceans* 52. 131–169. doi:10.1016/j.dynatmoce.2011.04.003, 2011.
- Giering, S. L. C., Sanders, R., Martin, A. P., Henson, S. A., Riley, J. S., Marsay, C. M., and Johns, D. G.: Particle flux in the oceans: Challenging the steady state assumption. *Global Biogeochemical Cycles*, 31(1), 159–171.
- 830 doi:10.1002/2016GB005424, 2017.
- González, H. E.: Distribution and abundance of minipellets around the Antarctic peninsula. Implications for protistan feeding behaviour, *Mar. Ecol. Prog. Ser.*, 90, 223–236, doi:10.3354/meps090223, 1992.
- González, H. E., Ortiz, V. C., and Sobarzo, M.: The role of faecal material in the particulate organic carbon flux in the northern Humboldt Current, Chile (23°S), before and during the 1997 – 1998 El Niño, *Journal of Plankton Research*, 22(3), 499–529,
- 835 doi:10.1093/plankt/22.3.499, 2000.
- Gorsky, G. and Fenaux, R.: The role of appendicularia in marine food webs, *The Biology of Pelagic Tunicates*, Oxford University Press, Oxford, 161–169, 1998.
- Gowing, M.M.: Abundance and feeding ecology of Antarctic phaeodarian radiolarians, *Marine Biology*, 103, 107–118. doi:10.1007/BF00391069, 1989.



- 840 Gruber, N., Lachkar, Z., Frenzel, H., Marchesiello, P., Münnich, M., McWilliams, J. C., Nagai, T. and Plattner, G.-K.: Eddy-induced reduction of biological production in eastern boundary upwelling systems. *Nature Geoscience*, 4(11), 787–792. doi:10.1038/ngeo1273, 2011.
- Henson, S. A., Sanders, R., Madsen, E., Morris, P. J., Le Moigne, F., and Quartly, G. D.: A reduced estimate of the strength of the ocean’s biological carbon pump. *Geophysical Research Letters*, 38(4), 10–14. doi:10.1029/2011GL046735, 2011.
- 845 Johnson, K. S., Plant, J. N., Dunne, J. P., Talley, L. D., and Sarmiento, J. L.: Annual nitrate drawdown observed by SOCCOM profiling floats and the relationship to annual net community production. *Journal of Geophysical Research: Oceans*, 122(8), 6668–6683. doi:10.1002/2017JC012839, 2017.
- Kelly, T.B, Goericke, R., Kahru, M., Song, M., and Stukel, M.R.: CCE II: Spatial and interannual variability in export efficiency and the biological pump in an eastern boundary current upwelling system with substantial lateral advection. *Deep-Sea Research I*, 140, 14–25. doi:10.1016/j.dsr.2018.08.007, 2018.
- 850 Kranz, S. A., Wang, S., Kelly, T. B., Stukel, M. R., Goericke, R., Landry, M.R., and Cassar, N.: Lagrangian studies of marine production: A multimethod assessment of productivity relationships in the California Current Ecosystem upwelling region. *Journal of Geophysical Research: Oceans*, 125, e2019JC015984. doi:10.1029/2019JC015984, 2020.
- Krause, M.: Vertical distributions of fecal pellets during FLEX ’76. *Helgolander Meeresunters*, 34(3), 313–327, doi:10.1007/BF02074125, 1981.
- 855 Kwon, E. Y., Primeau, F., and Sarmiento, J. L.: The impact of remineralization depth on the air–sea carbon balance. *Nature Geoscience*, 2, 630. doi:10.1038/ngeo612, 2009.
- Lam, P.J., Bishop, J.K.B., Henning, C. C., Marcus, M.A., Waychunas, G. A. and Fung, I.Y.: Wintertime phytoplankton bloom in the Subarctic Pacific supported by Continental Shelf Iron., *Global Biogeochemical Cycles*. 20, 12pp. GB1006, doi:10.1029/2005GB002557, 2006.
- 860 Lam, P. J., and Bishop, J. K. B.: High biomass, low export regimes in the Southern Ocean. *Deep-Sea Research Part II: Topical Studies in Oceanography*, 54(5–7), 601–638, doi:10.1016/j.dsr2.2007.01.013, 2007.
- Li, Z., and Cassar, N., Satellite estimates of net community production based on O₂/Ar observations and comparisons to other estimates, *Global Biogeochemical Cycles*, 30, 735–752, doi: 10.1002/2015GB005314, 2016.
- 865 Lutz, M., Caldeira, K., Dunbar, R., and Behrenfeld, M.: Seasonal rhythms of net primary production and particulate organic carbon flux to depth describe the efficiency of biological pump in the global ocean, *J. Geophys. Res.-Oceans*, 112, C10011, doi:10.1029/2006JC003706, 2007.



- Lynn, R. J. and Simpson, J. J.: The California Current System: The Seasonal Variability of its Physical Characteristics, *Journal of Geophysical Research: Oceans*, 92 (12), 12947–12966, doi:10.1029/JC092iC12p12947, 1987.
- 870 Madin, L.P., and Purcell, J.E.: Feeding, metabolism and growth of *Cyclosapa Bakeri* in the subarctic Pacific, *Limnology and Oceanography*, 37(6), 1236-1251, doi:10.4319/lo.1992.37.6.1236, 1992.
- Marsay, C. M., Sanders, R. J., Henson, S., Pabortsava, K., and Achterberg, E.P.: Attenuation of sinking particulate organic carbon flux through the mesopelagic ocean. *Proceedings of the National Academy of Sciences*, 112 (4) 1089–1094, doi:10.1073/pnas.1415311112, 2015.
- 875 Martin, J.H., Knauer, G.A., Karl, D.M., and Broenkow, W.W.: VERTEX: carbon cycling in the northeast Pacific. *Deep Sea Research Part A. Oceanographic Research Papers*, 34(2), 267–285. doi:10.1016/0198-0149(87)90086-0, 1987.
- McPhee-Shaw, E.E., Sternberg, R.W., Mullenbach, B. and Ogston, A.S.: Observations of intermediate nepheloid layers on the northern California continental margin, *Continental Shelf Research*, 24(6), 693-720, doi:10.1016/j.csr.2004.01.004, 2004.
- Ohman, M., Barbeau, K., Franks, P., Goericke, R., Landry, M., and Miller, A.: Ecological Transitions in a Coastal Upwelling
880 Ecosystem. *Oceanography*, 26(3), 210–219. doi:10.5670/oceanog.2013.65, 2013.
- Omand, M. M., Asaro, E.A., Lee, C.M., Perry, M.J., Briggs, N., Cetinić, I., and Mahadevan, A.: Eddy-driven subduction exports particulate organic carbon from the spring bloom, *Science*, 348, 222-225. doi: 10.1126/science.1260062, 2015.
- Pak, H., Zaneveld, R. V. and Kitchen J.: Intermediate Nepheloid Layers Observed off Oregon and Washington. *Journal of Geophysical Research: Oceans*, 85(11), 6697-6708, doi.org/10.1029/JC085iC11p06697, 1980.
- 885 Passow, U., and Carlson, C.A.: The biological pump in a high CO₂ world. *Marine Ecology Progress Series*, 470, 249–271. doi:10.3354/meps09985, 2012.
- Pomeroy, L.R., Hanson, R.B., McGillivray, P.A., B.F. Sherr, D. Kirchman, D., and Deibel, D.: Microbiology and chemistry of fecal products of pelagic tunicates: rates and fates. *Bull. Mar. Sci.*, 35 (3), 426–439, 1984.
- Saba, G. K., and Steinberg, D. K.: Abundance, composition, and sinking rates of fish fecal pellets in the santa barbara channel.
890 *Scientific Reports*, 2, 1–6. doi:10.1038/srep00716, 2012.
- Sasaki, H., Hattori, H., and Nishizawa, S.: Downward flux of particulate organic matter and vertical distribution of calanoid copepods in the Oyasio Waters in the summer. *Deep-Sea Research Part A*, 35, 505–515. doi:10.1016/0198-0149(88)90128-8, 1988.
- Schneider, N., Lorenzo, E.D., and Niler, P. P.: Salinity Variations in the Southern California Current. *J. Phys. Ocean.* 35,
895 1421–1436. doi:10.1175/JPO2759.1, 2005.



- Siegel, D. A., Buesseler, K. O., Doney, S. C., Sailley, S. F., Behrenfeld, M. J., and Boyd, P. W.: Global assessment of ocean carbon export by combining satellite observations and food-web models. *Global Biogeochemical Cycles*, 28, 181–196. doi:10.1002/2013GB004743, 2014.
- Siegel, D. A., Buesseler, K. O., Behrenfeld, M. J., Benitez-nelson, C. R., Boss, E., Brzezinski, M. A., Burd, A., Carlson, C. A., D'Asaro, E. A., Doney, S. C., Perry, M. J., Stanley, R. H. R., and Steinberg, D. K.: Prediction of the Export and Fate of Global Ocean Net Primary Production : The EXPORTS Science Plan, 3(March), 1–10. doi:10.3389/fmars.2016.00022, 2016.
- Siegelman-Charbit, L., Koslow, J. A., Jacox, M. G., Hazen, E. L., Bograd, S. J., and Miller, E. F.: Physical forcing on fish abundance in the southern California Current System. *Fisheries Oceanography*, 27, 475–488. doi:10.1111/fog.12267, 2018.
- Silver, M. W., Coale, S. L., Pilskaln, C. H., and Steinberg, D. R.: Giant aggregates: Importance as microbial centers and agents of material flux in the mesopelagic zone. *Limnology and Oceanography*, 43(3), 498–507. doi:10.4319/lo.1998.43.3.0498, 1998.
- Smetacek, V.S.: Zooplankton standing stock, copepod faecal pellets and particulate detritus in Kiel bight, *Estuarine and Coastal Marine Science*, 11, 477–490, doi: 10.1016/S0302-3524(80)80001-6, 1980.
- Stanley, R. H. R., Doney, S. C., Jenkins, W. J., and Lott, D. E.: Apparent oxygen utilization rates calculated from tritium and helium-3 profiles at the Bermuda Atlantic Time-series Study site. *Biogeosciences*, 9(6), 1969–1983. doi:10.5194/bg-9-1969-2012, 2012.
- Stemmann, L., Prieur, L., Legendre, L., Taupier-Letage, I., Picheral, M., Guidi, L. and Gorsky, G.: Effects of frontal processes on marine aggregate dynamics and fluxes: an interannual study in a permanent geostrophic front (NW Mediterranean), *Journal of Marine Systems*, 70, 1–20. doi:10.1016/j.jmarsys.2007.02.014, 2008.
- Steinberg, D. K., Van Mooy, B.A.S., Buesseler, K.O., Boyd, P.W., Kobari, T. and Karl, D.M.: Bacterial vs. zooplankton control of sinking particle flux in the ocean's twilight zone. *Limnology and Oceanography*. 53(4): 1327–1338. doi:10.4319/lo.2008.53.4.1327, 2008.
- Stukel, M. R., Ohman, M. D., Benitez-Nelson, C. R., and Landry, M. R.: Contributions of mesozooplankton to vertical carbon export in a coastal upwelling system. *Marine Ecology Progress Series*, 491, 47–65. doi:10.3354/meps10453, 2013.
- Stukel, M. R., Asher, E., Couto, N., Schofield, O., Strebel, S., Tortell, P., and Ducklow, H. W.: The imbalance of new and export production in the western Antarctic Peninsula, a potentially “leaky” ecosystem. *Global Biogeochemical Cycles*, 29, 1400–1420. doi:10.1002/2015GB005211, 2015.
- Stukel, M. R., Song, H., Goericke, R., and Miller, A. J.: The role of subduction and gravitational sinking in particle export , carbon sequestration , and the remineralization length scale in the California Current Ecosystem, *Limnology and Oceanography*, 63, 363–383. doi:10.1002/lno.10636, 2018.



Turner, J.T.: Progress in Oceanography Zooplankton fecal pellets , marine snow , phytodetritus and the ocean ' s biological pump. *Progress in Oceanography*, 130, 205–248. doi:10.1016/j.pocean.2014.08.005, 2015.

Whitmore, B. M., Nickels, C. F. and Ohman, M. D.: A comparison between Zooglider and shipboard net and acoustic mesozooplankton sensing systems. *Journal of Plankton Research* 41, 521-533 doi:10.1093/plankt/fbz033, 2019.

930 Yao, X., and Schlitzer, R.: Assimilating water column and satellite data for marine export production estimation. *Geoscientific Model Development*, 6(5), 1575–1590. doi:10.5194/gmd-6-1575-2013, 2013.

Data Availability.

935



Table 1. Carbon Flux Explorer deployments during CCE-LTER process study P1706 June 2 – July 1 2017.

Cycle ¹	Location ²	CFE Name	Deploy UTC date ³	Deploy Day ⁴	Deploy Latitude	Deploy Longitude	Recovery Day ⁴	Recovery Latitude	Recovery Longitude
1	L1	CFE-2-Cal	20170609	159.9917	35.0739	-121.1281	160.8694	35.0187	-121.1653
1	L1	CFE-1	20170610	161.1215	35.0000	-121.1686	162.4806	34.9088	-121.2132
1	L1	CFE-3	20170610	161.0818	35.0000	-121.1686	162.4701	34.9047	-121.1995
1	L1	CFE-2-Cal	20170611	161.9999	34.9396	-121.2031	162.5528	34.9204	-121.2256
1	L1	CFE-4-Cal	20170611	162.0197	34.9348	-121.1946	162.5819	34.9061	-121.2074
2	L2a	CFE-1	20170613	164.1597	34.7391	-121.8349	167.4826	34.9788	-122.4062
2	L2a	CFE-3	20170613	164.1782	34.7391	-121.8349	167.4972	34.9613	-122.4558
2	L2a	CFE-2-Cal	20170614	164.9700	34.7771	-122.0572	166.0451	34.8913	-122.3356
2	L2a	CFE-4-Cal	20170614	164.9822	34.7742	-122.0587	165.9201	34.8850	-122.3084
2	L2b	CFE-2-Cal	20170616	166.5817	34.7098	-122.3004	167.5375	34.7051	-122.4151
2	L2b	CFE-4-Cal	20170616	166.5952	34.7091	-122.2998	167.5500	34.7082	-122.4188
3	L3	CFE-1	20170619	169.9880	34.2382	-123.1001	170.8958	34.1973	-123.0502
3	L3	CFE-2-Cal	20170619	170.1173	34.2275	-123.1480	170.9007	34.1716	-123.0759
3	L3	CFE-1	20170621	171.1496	34.1129	-122.9885	172.5139	34.0782	-122.8477
3	L3	CFE-2-Cal	20170621	171.1150	34.1137	-122.9939	171.9257	34.0773	-122.8891
3	L3	CFE-4-Cal	20170621	171.1310	34.1086	-122.9823	171.9243	34.0734	-122.8689
4	L4	CFE-1	20170623	174.1295	34.4032	-123.0964	176.5160	34.4452	-123.0978
4	L4	CFE-2-Cal	20170623	174.2182	34.4070	-123.0958	174.9417	34.4240	-123.0342
4	L4	CFE-4-Cal	20170623	174.1028	34.4024	-123.1040	174.9174	34.4294	-123.0595
4	L4	CFE-2-Cal	20170625	175.0991	34.4218	-123.0168	176.5340	34.4521	-123.0161
4	L4	CFE-4-Cal	20170625	175.1102	34.4221	-123.0133	176.5132	34.4835	-122.9888

1. CCE-LTER Cycle number; 2. Location Number used in this paper; 3. Deploy Date (YYYYMMDD); 4. Day – year days since Jan 1 2017 0000 UTC. Jan 1 2017 at 1200 UTC= 0.5.



940 Table 2. Martin Curve Fits to Attenuance Flux

Location	Zref	size bin	Martin Curve 'b'	b-Error	Intercept	intercept Error	SE y	R2	n
1	50	30-100	-1.907	0.587	-0.080	0.302	0.132	0.967	4
1	50	100-200	-1.137	0.675	-0.075	0.347	0.152	0.887	4
1	50	200-400	-0.376	0.708	0.305	0.364	0.159	0.439	4
1	50	400-1000	-0.280	0.780	0.142	0.401	0.175	0.263	4
1	50	>1000	0.211	1.148	1.307	0.590	0.258	0.086	4
1	50	Total	0.098	1.052	1.414	0.541	0.236	0.023	4
2	100	30-100	-0.633	0.152	-0.971	0.064	0.033	0.980	4
2	100	100-200	-0.712	0.309	-0.474	0.130	0.067	0.936	4
2	100	200-400	-1.710	0.858	0.783	0.360	0.187	0.917	4
2	100	400-1000	0.617	0.467	-0.176	0.196	0.101	0.829	4
2	100	>1000	1.439	0.910	0.599	0.382	0.198	0.874	4
2	100	Total	0.867	0.479	0.972	0.201	0.104	0.901	4
3	100	30-100	-1.691	0.981	-0.933	0.417	0.194	0.892	4
3	100	100-200	-1.668	0.474	-0.481	0.202	0.094	0.972	4
3	100	200-400	-1.125	0.429	-0.231	0.182	0.085	0.950	4
3	100	400-1000	-0.176	1.398	-0.529	0.595	0.277	0.042	4
3	100	>1000	-0.319	0.421	0.542	0.179	0.083	0.614	4
3	100	Total	-0.391	0.426	0.655	0.181	0.084	0.700	4
4	100	30-100	-0.785	0.430	-0.827	0.180	0.091	0.902	4
4	100	100-200	-0.488	0.804	-0.582	0.336	0.170	0.506	4
4	100	200-400	-0.423	0.733	-0.223	0.306	0.155	0.480	4
4	100	400-1000	-0.315	0.699	0.238	0.292	0.147	0.360	4
4	100	>1000	-0.206	1.035	1.461	0.442	0.220	0.099	4
4	100	Total	-0.269	0.839	1.502	0.351	0.177	0.222	4



Table 3. Martin Curve Fits to Number Flux

Location	Zref	size bin	Martin		intercept		SE _y	R ²	n
			Curve 'b'	b-Error	Intercept	Error			
1	50	30-100	-1.866	0.605	6.665	0.311	0.136	0.964	4
1	50	100-200	-1.471	0.722	5.750	0.371	0.162	0.920	4
1	50	200-400	-0.810	0.656	5.172	0.337	0.147	0.809	4
1	50	400-1000	-0.987	0.662	4.475	0.340	0.149	0.861	4
1	50	>1000	-0.052	1.008	3.936	0.518	0.226	0.007	4
1	50	Total	-1.717	0.614	6.725	0.315	0.138	0.956	4
2	100	30-100	-0.615	0.174	5.817	0.073	0.038	0.972	4
2	100	100-200	-0.484	0.254	5.068	0.107	0.055	0.909	4
2	100	200-400	-1.455	0.942	5.359	0.395	0.205	0.869	4
2	100	400-1000	0.195	0.446	3.958	0.187	0.097	0.347	4
2	100	>1000	1.146	0.784	3.541	0.329	0.170	0.856	4
2	100	Total	-0.654	0.101	5.999	0.042	0.022	0.991	4
3	100	30-100	-1.336	0.741	5.584	0.315	0.147	0.900	4
3	100	100-200	-2.328	0.934	5.417	0.397	0.185	0.945	4
3	100	200-400	-1.327	0.785	4.473	0.334	0.155	0.888	4
3	100	400-1000	-0.586	0.814	3.617	0.346	0.161	0.590	4
3	100	>1000	-0.311	0.619	3.323	0.263	0.122	0.412	4
3	100	Total	-1.520	0.798	5.812	0.340	0.158	0.909	4
4	100	30-100	-0.720	0.506	5.918	0.211	0.107	0.849	4
4	100	100-200	-0.500	0.815	5.189	0.341	0.172	0.510	4
4	100	200-400	-0.337	0.916	4.691	0.383	0.193	0.273	4
4	100	400-1000	-0.238	0.979	4.254	0.409	0.206	0.140	4
4	100	>1000	-0.190	0.977	4.098	0.417	0.208	0.095	4
4	100	Total	-0.643	0.595	6.026	0.249	0.125	0.764	4

Notes: errors are 95% confidence intervals.



Figures.

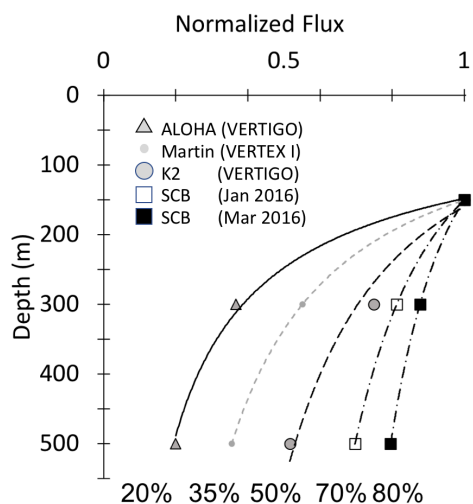


Figure 1. Martin curves normalized to 150 m. Representative data from Martin et al. (1987), Buessler et al., (2007) and Bishop et al., (2016). “b” values of lines from left to right are: -1.33 (Stn. ALOHA), -0.86 (VERTEX I), -0.51 (Stn. K2), -0.19 and -0.3 (March and Jan 2016, Santa Cruz Basin). Transport efficiencies between 150 and 500 m range from 20% (ALOHA) to 80% (Santa Cruz Basin).

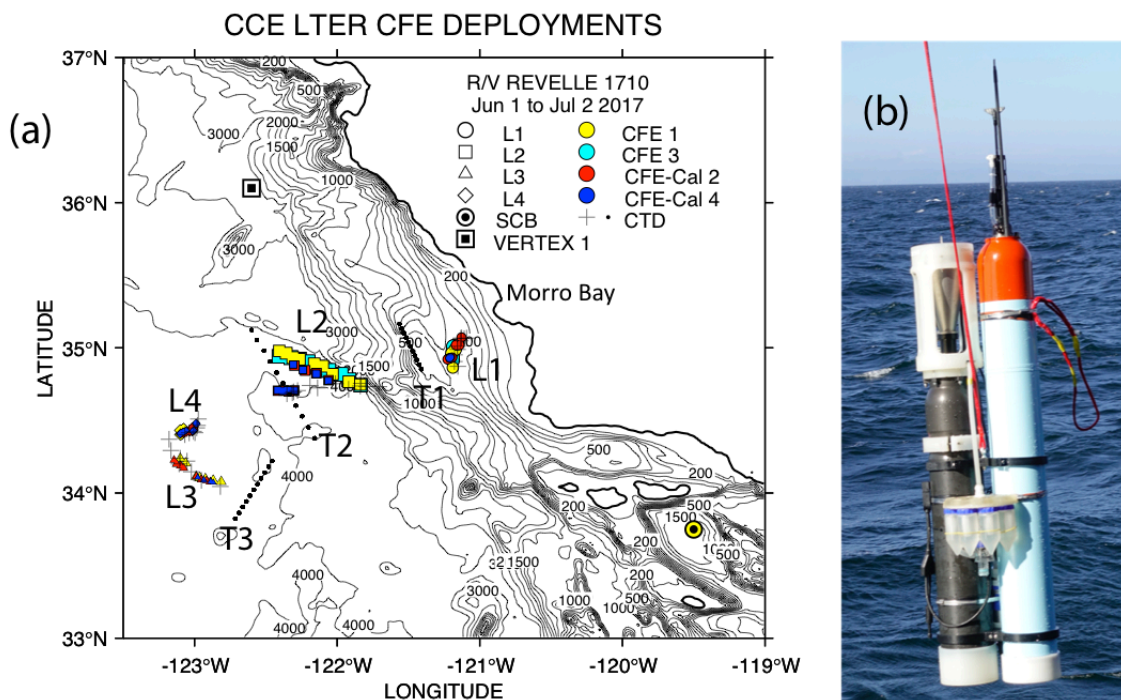


Figure 2. (a) CFE and CTD deployments at locations L1 to L4. The CTD stations were close to a drifting surface drogued productivity array. For the majority of stations, the CTDs and CFEs were close to one another. However, at L2, the CFEs diverged to the west-north-west of the drogued drifters. Dots depict locations of cross-filament CTD particle-optics transects T1, T2, and T3. T1 preceded work at L1; T2 was occupied after completion of sampling at L2. T3 was completed after work at L4. Data from transects shown in Fig. 11. (b) CFE-Cal during recovery.

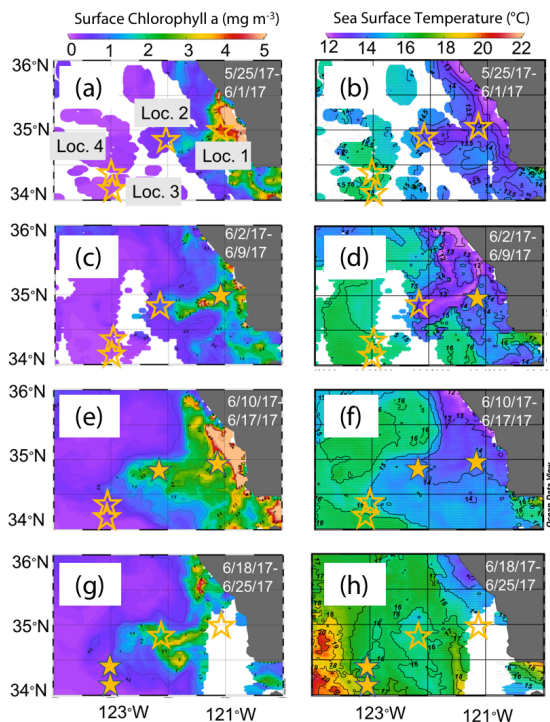


Figure 3. Remotely sensed surface chlorophyll (a,c,e,g) and sea surface temperature (SST) (b,d,f,h) maps of the study area from late May to the end of June 2017. All images are from 4 km resolution, 8-day averaged data from NASA Ocean Color from SNPP VIIRS. The stars represent locations 1 to 4 where CFEs were deployed. Stars are filled in the panels most closely corresponding to the time of observations.

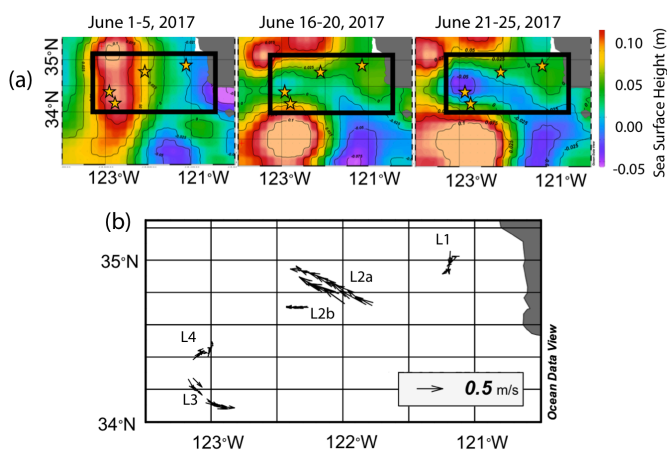


Figure 4. (a) Average sea surface height from June 1-5, 16-20 and 21-25 2017. In the beginning of June, sea surface height was low near the shore due to Ekman transport, and higher off the coast. As the filament developed and moved to the west, a sea surface trough formed extending 200 km offshore and was first apparent in the June 16-20 map; it deepens in the June 21-25 map, indicating the formation of a cyclonic eddy; Anti-cyclonic eddies are present to the north and south. Stars represent positions of each location. (b) Velocity vectors for all CFE dives to depths of 500 m. The CFE motions were fastest at locations L2 and L3, where the CFEs were deployed near the edges of the cyclonic eddies and slowest at L1 inshore and at L4 which was located near the center of the cyclonic eddy.

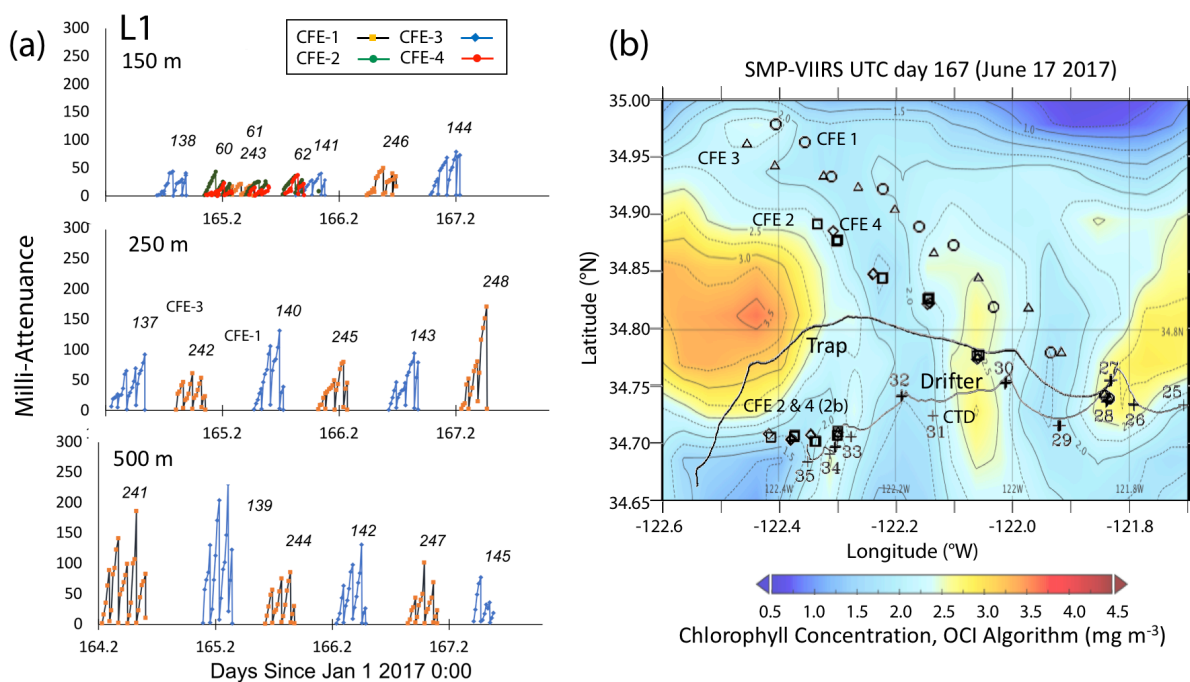


Figure 5. (a). Raw attenuation time series for all CFEs deployed at L2. See Fig. 2 for deployment context. *Italicized numbers* are the dive numbers corresponding to the data. The *mATN* timeseries scales with flux as timing is constant. **(b).** Map showing deployment and trajectories of CFEs, CTD station locations, and tracks of the productivity drifter and sediment trap array during the intensive studies at L2. The overlay is the SMPP-VIIRS chlorophyll field for June 17 2017– during the later stages of sampling at this location.

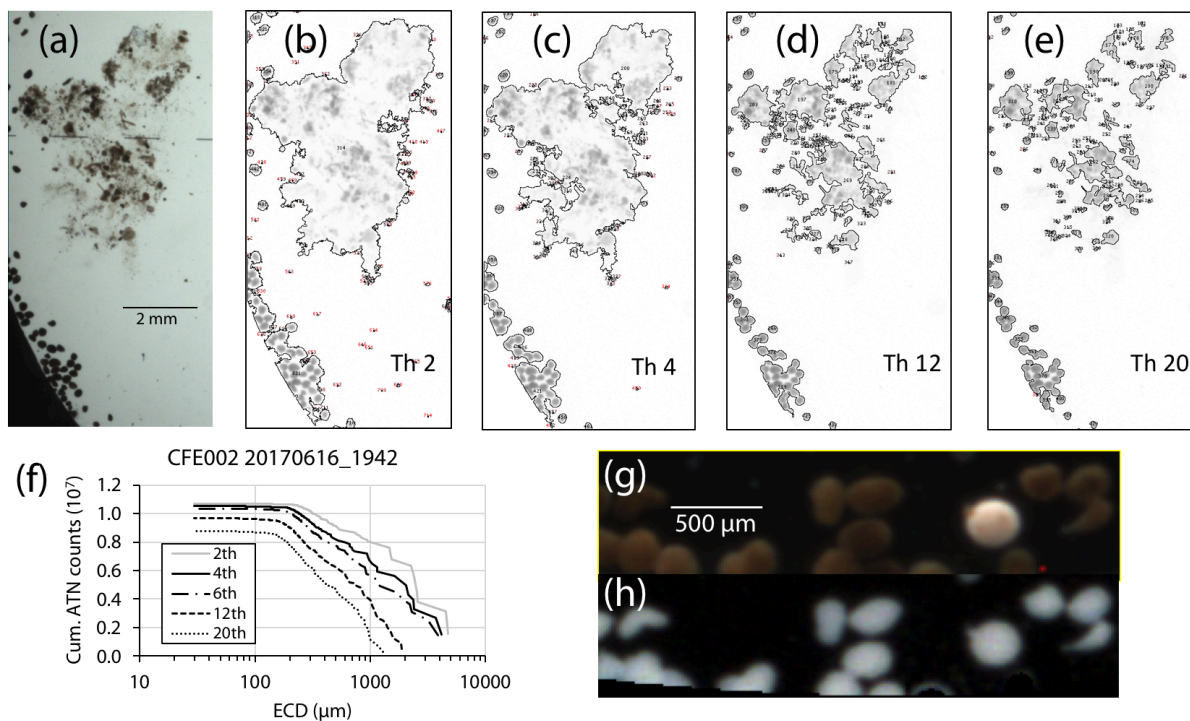


Figure 6. Top: (a) Segment of a CFE-2 transmitted light image June 2017 at 1942 UTC; depth 150 m. Panels (b – e): ImageJ particle outline maps at attenuation thresholds of 0.02, 0.04, 0.12, and 0.20, superimposed on the attenuation image for the sample. Darker greys denote higher attenuation. We found that touching fecal pellets could not be separated even at a threshold of 0.20 ATN. At thresholds >0.06, large low-density aggregates are seen as highly fragmented and the contribution of smaller particles is reduced. Lower: (f) Particle size attenuation count distributions as a function of threshold. (g) Magnified image under dark field illumination. Olive colored fecal pellets are readily distinguished from an unidentified egg. (h) Attenuance map of the same view.

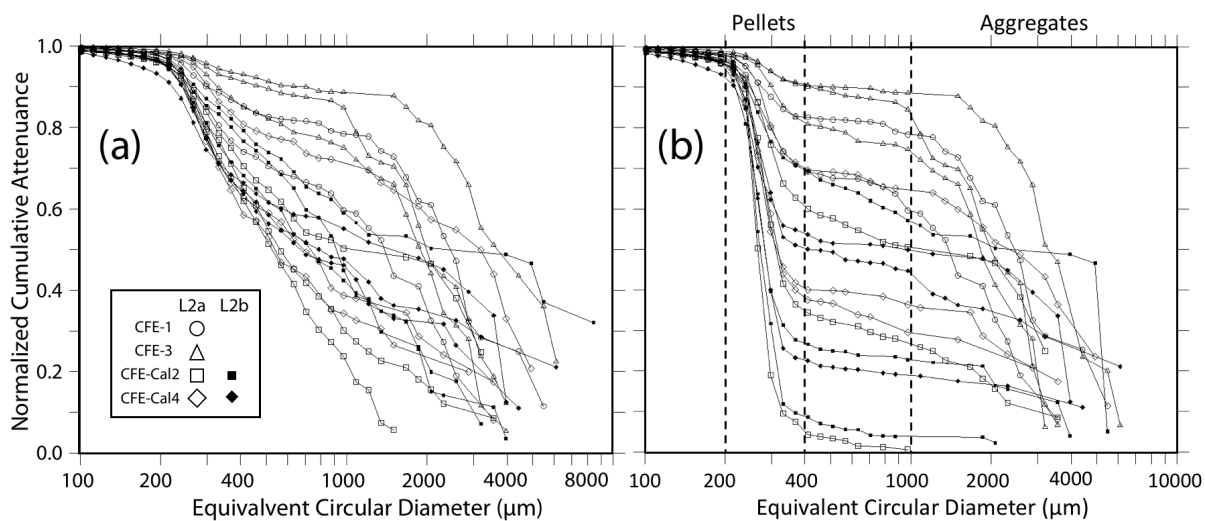


Figure 7. Processed size distribution data for CFEs 1, 2, 3 and 4 deployed near 150 m at L2. Normalized Cumulative Attenuance Flux is plotted against Equivalent Circular Diameter (in μm). (a) Original data from ImageJ and (b) after secondary processing to correct for touching particles. Boundaries for reduced size categories are 30–100 μm (not shown), 100–200 μm , 200–400 μm , 400–1000 μm , and >1000 μm are indicated in (b). Open and closed symbols denote data from L2a and L2b, respectively.

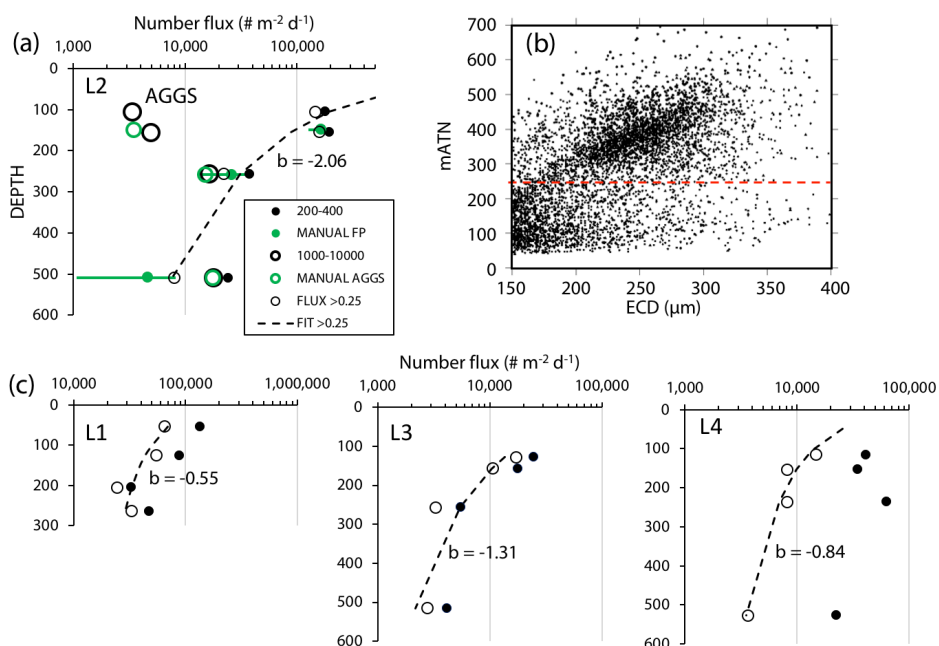


Figure 8. (a) Profile of aggregate and pellet number fluxes determined by Method 3 (black large open circles and filled circles) and by manual counting (green large open circles and filled circles) at Location L2. The small open circles represent number flux of 200–400 μm particles with average attenuation >0.25. These data agree closely with manually enumerated pellet counts. (b) Plot of average particle attenuation vs. equivalent circular diameter (ECD). The red dashed line denotes the lower boundary of the cluster of >0.25 ATN particles. (c). Profiles of 200–400 μm total particle number fluxes and for >0.25 ATN particles at L1, L3, and L4. Dashed lines are Martin fits to the adjusted data. In all cases, fluxes of fecal pellets decrease with depth.

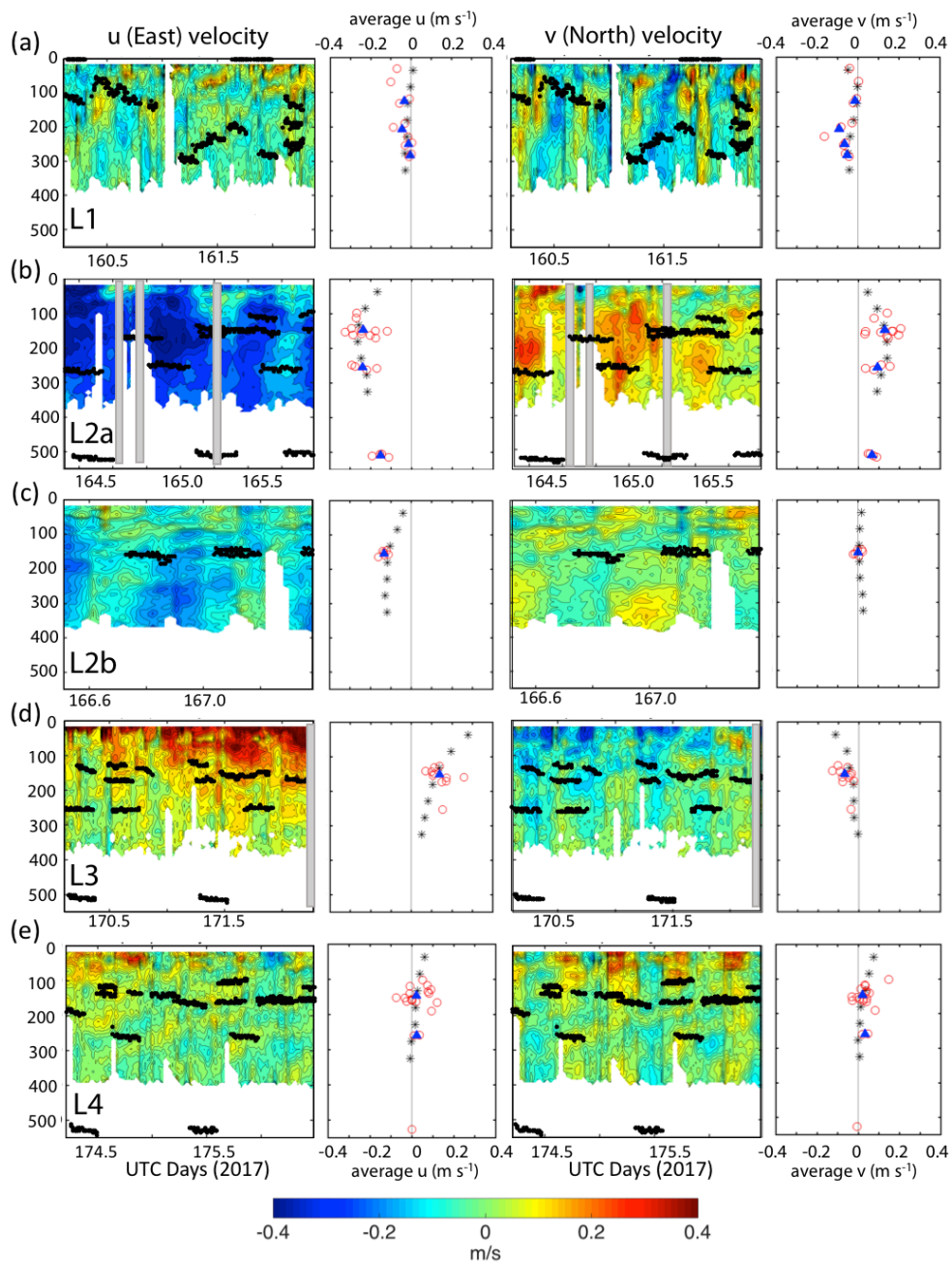


Figure 9. Thirty-second averaged current velocities in u (East positive) and v (North positive) directions from 150 kHz narrow band ADCP data. CFE depths during flux measurements are shown. Profiles denoted by black asterisks to right of each contour plot are averaged ADCP velocities for the entire time span. Red points represent average CFE velocities over the course of each dive. Filled blue triangles are the averaged CFE velocities for all dives at a given depth. Panels (a), (b), (c), (d), and (e) Locations 1, 2a, 2b, 3 and 4 respectively.



960

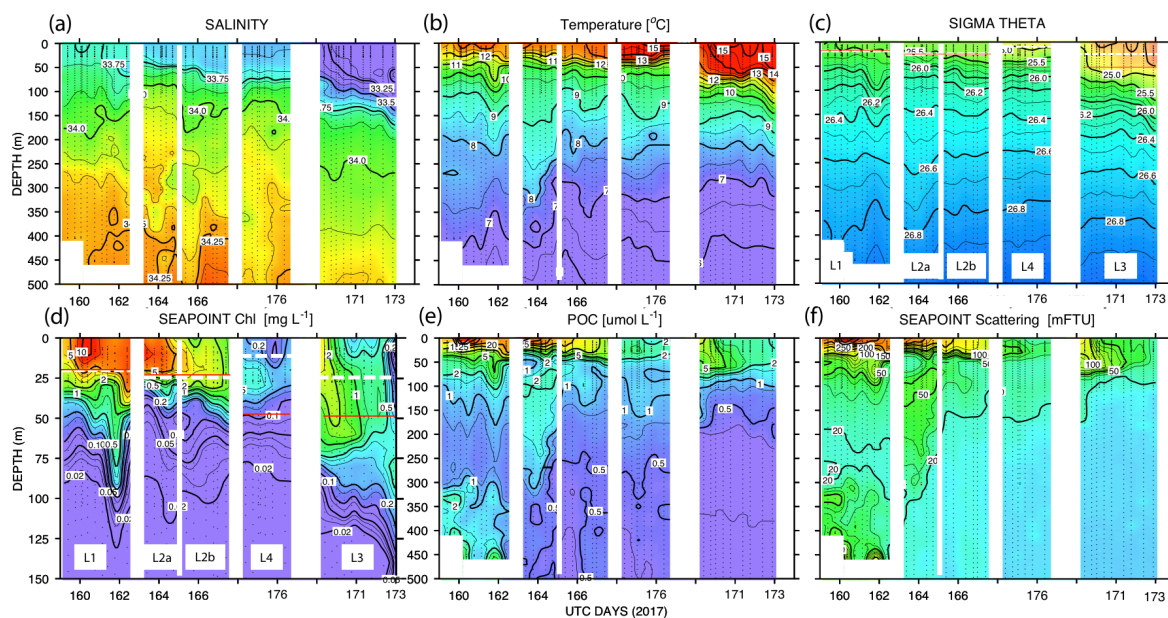


Figure 10. (a) Salinity, (b) temperature, (c) sigma theta (σ_θ), (d) chlorophyll fluorescence, (e) transmissometer derived POC, and (f) turbidity timeseries from CTD casts. The time axis (in UTC days since Jan 1 0000h 2017) has been reordered so that L1, L2, and L4 are grouped. L3 is shifted to the right side of each panel. The white dashed line and red line (c) and (d) denote averaged 24 h mixed layer depths and euphotic zone depths, respectively. The chlorophyll fluorescence (d) depth axis is 150 m; limit of detection was 0.02 units.

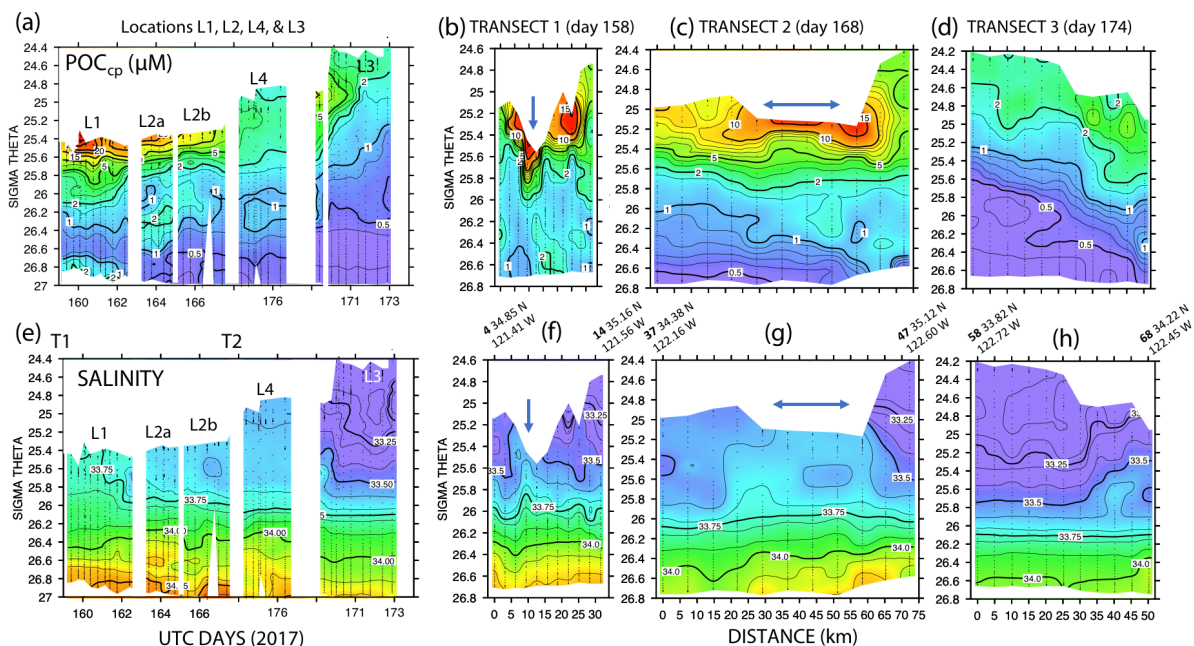


Figure 11. (a) Transmissometer particulate organic carbon (POC) and (e) salinity – potential density time series during the intensive studies at L1, L2a, L2b, L4, and L3. Also shown are cross-filament transects T1, T2, and T3 for POC (b), (c), (d) and salinity (f), (g), (h). Transect locations are shown in Fig. 2. Transect T1 (UTC day 158) was located between L1 and L2; T2 (day 168) was sited between L2 and L4; and T3 crossed the outer edge of the filament on day 174 after completion of work at L4. Distances in kilometers. UTC days as defined in Fig. 10. The arrows in (f) and (g) indicate the high salinity surface water in the filament; its scale was ~5 km wide at T1, it was ~25 km wide at T2.

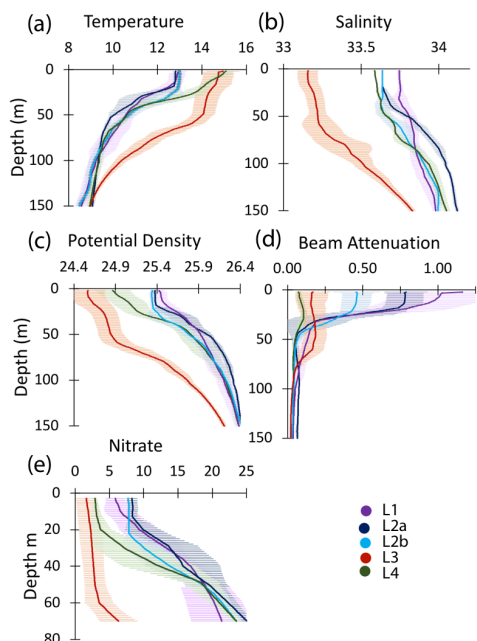


Figure 12. Profiles of averaged T, S, potential density, beam attenuation coefficient (650nm), and nitrate in the upper 150 m at locations L1, L2a, L2b, L3, and L4. Error bars are ± 1 S.D.

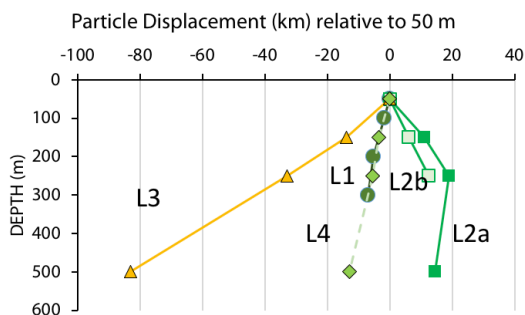


Figure 13. Displacements (in kilometers) in the direction of motion of the filament for particles with a hypothetical sinking rate of 100 m d^{-1} as they sink from 50 m. Extreme displacements were calculated for transitional waters (L3) where sinking particles lagged behind the surface layer by as much as 85 km. Sinking particles would lead the surface layer by 20 km at a depth of 250 m at L2a. Calculated from ADCP fields in Fig. 8.

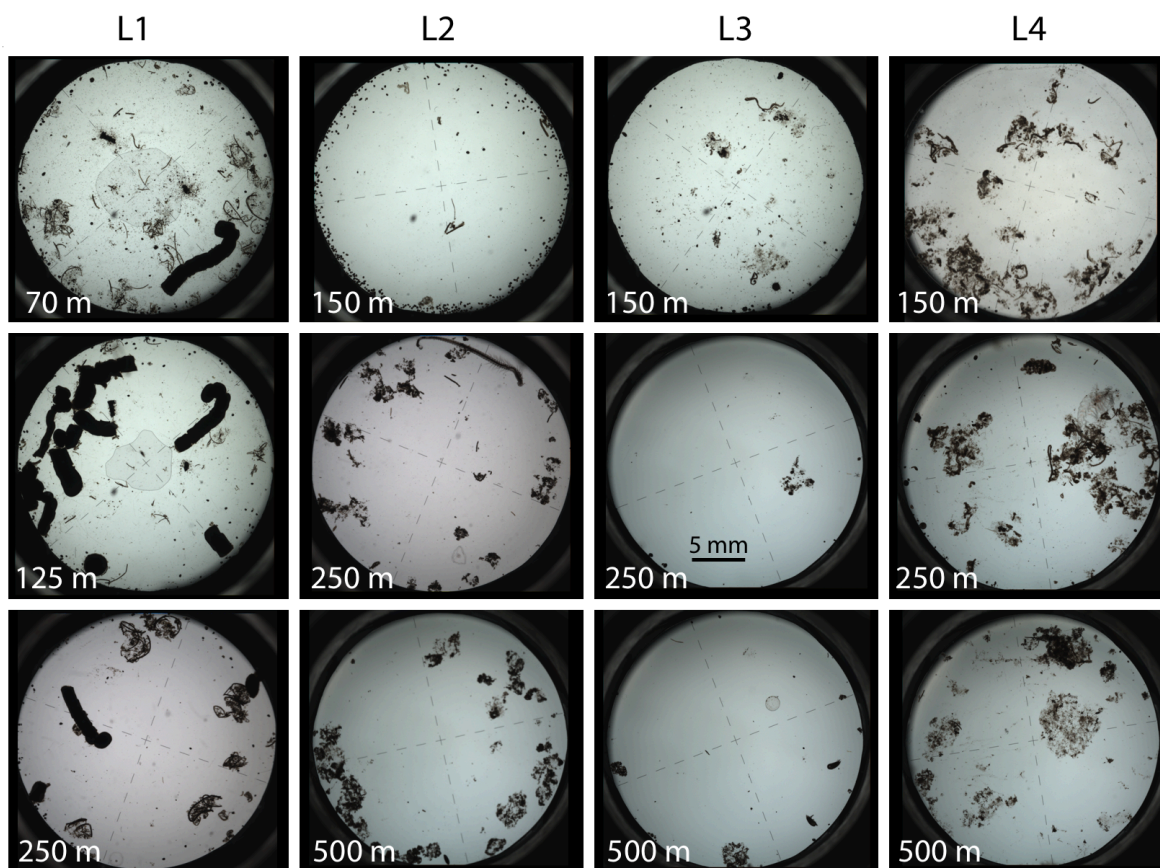


Figure 14. Representative transmitted light imagery of particles sampled by the CFEs at locations L1, L2, L3 and L4. The top row of images is for material captured at ~100 m. Middle row, particles captured near 250 m (150 m at L1). Bottom row are images of particles captured near 500 m (300 m at L1). Dashes in the images are 1 mm long.



985

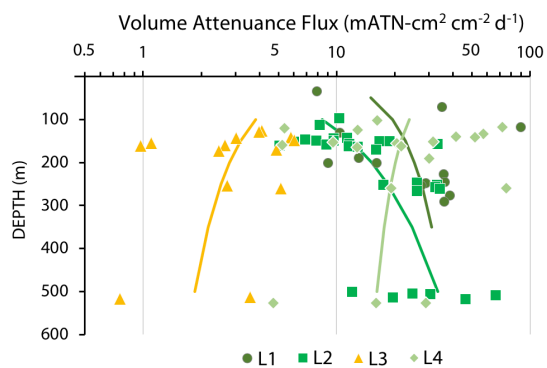


Figure 15. Volume Attenuance Flux (VAF, in units of $\text{mATN-cm cm}^{-2} \text{d}^{-1}$) for all CFE dives from in-filament locations L1 (olive circles), L2 (green squares), and L4 (light green diamonds), and in waters outside of the filament at L3 (orange triangles). The curves denote Martin function fits to the data with b values $+0.37$, $+0.85$, -0.45 , and -0.24 for L1–L4, respectively.

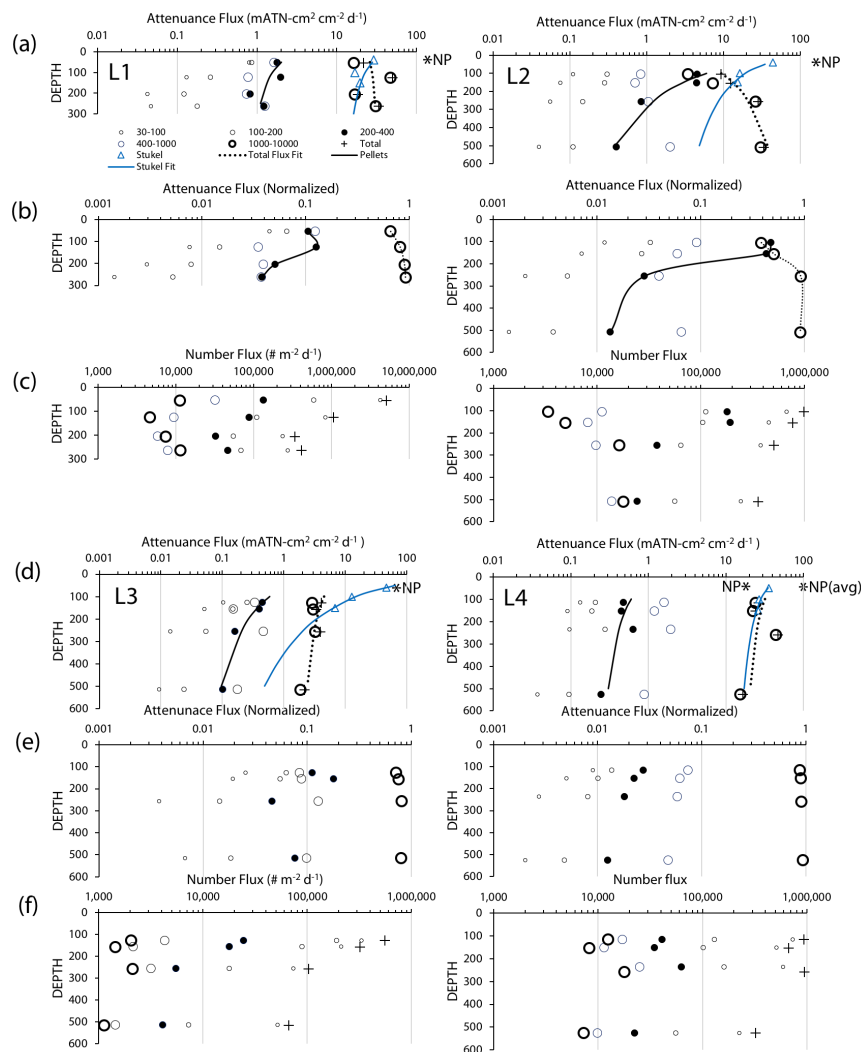


Figure 16. (a) Volume Attenuance Flux (VAF, in units of $\text{mATN-cm cm}^{-2} \text{d}^{-1}$) for 30-100 μm , 100-200 μm , 200-400 μm , 400-1000 μm , >1000-10000 μm size categories and total. Symbol size denotes size class. Filled circles correspond to the size category dominated by fecal pellets, heavy outlined circles are the >1000-10000 μm size category dominated by aggregates; curves are Martin Curve fits for 200-400 μm and Total flux categories. (b) VAF data normalized by total flux for the 5 size categories. Lines pass through the data for pellets and aggregate fractions. (c) Number fluxes (NF) ($\# \text{m}^{-2} \text{d}^{-1}$) for 5 size categories and total. Left column (a–c) are location L1. Right column (a–c) are for L2. (d), (e), (f) are VAF, normalized VAF, and number flux profiles as defined for (a), (b), and (c). Left and right columns for (d–f) correspond to data from locations L3 and L4, respectively. Blue Triangles in (a) and (d) show organic carbon flux ($\text{mmol C m}^{-2} \text{d}^{-1}$) from Kranz et al. (2020); the blue line is a Martin Curve fit to the trap data. A scaling factor of 0.97 converts VAF to carbon flux units. Asterisks denote measured values of euphotic zone New Production reported by Kranz et al. (2020). NP(avg) represents NP calculated for the 9 day period between occupations of L2b and L4.

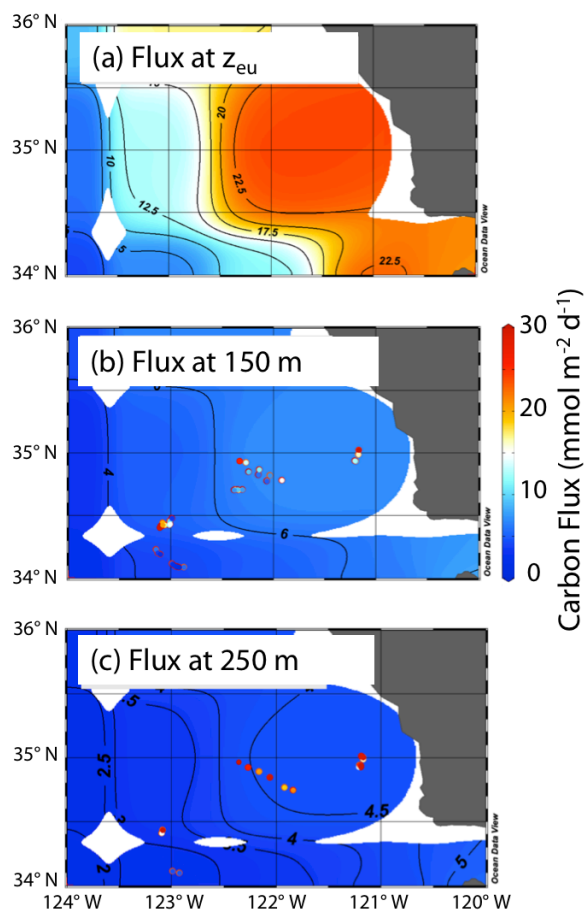


Figure 17. (a) Euphotic Zone Carbon Export for climatological averaged June from Siegel et al. (2014). (b) fluxes calculated for 150 m using Eqn (1) and the b value from VERTEX I (-0.83; Martin et al., 1987). The euphotic zone depth (z_{eu}) used for the calculation was June climatology from NASA VIIRS. (c) Carbon flux extrapolated for 250 m using the same method. The contour plots (b) and (c) are overlain using CFE carbon flux values from between 100 and 200m and between 200 and 300m. The CFE fluxes are far higher than model predictions at depth.

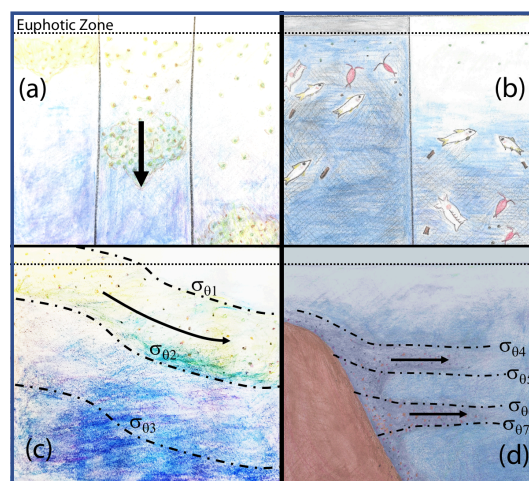


Figure 18. Cartoon depictions of four different mechanisms which could lead to flux profiles that do not decrease with depth.



990

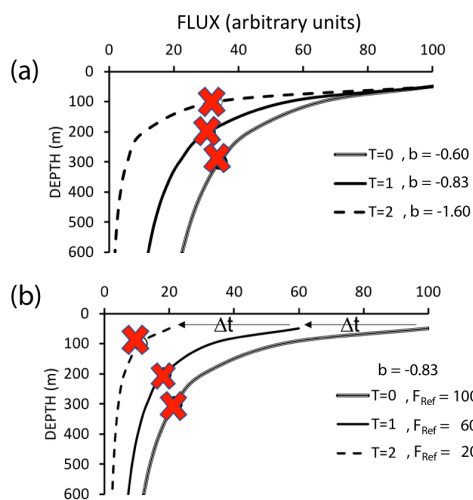


Figure 19. Scenarios which could lead to flux not systematically decreasing with depth. (a) depicts constant flux at the reference depth, with time variant values of the Martin b parameter. (b) depicts a scenario with constant Martin b , but decreasing flux at the reference depth over time (after Giering et al., 2016). Red marks indicate sampling points in both figures, illustrating how temporal delay could lead to observations of increasing flux with depth.

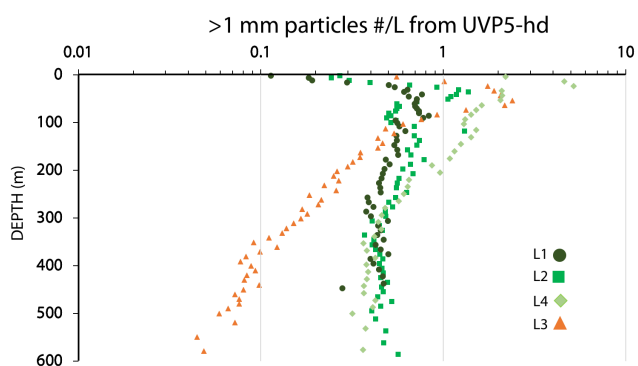


Figure 20. Particle number concentrations for >1.024 mm size material from UVP5hd profiles from averaged CTD casts at filament locations L1 (dark olive circles), L2 (green squares), L4 (light green diamonds), and outside of the filament at L3 (orange triangles). Aggregate numbers were more abundant in the waters beneath the filament than in transitional waters below 100m, consistent with CFE observations.



Appendix A.

995

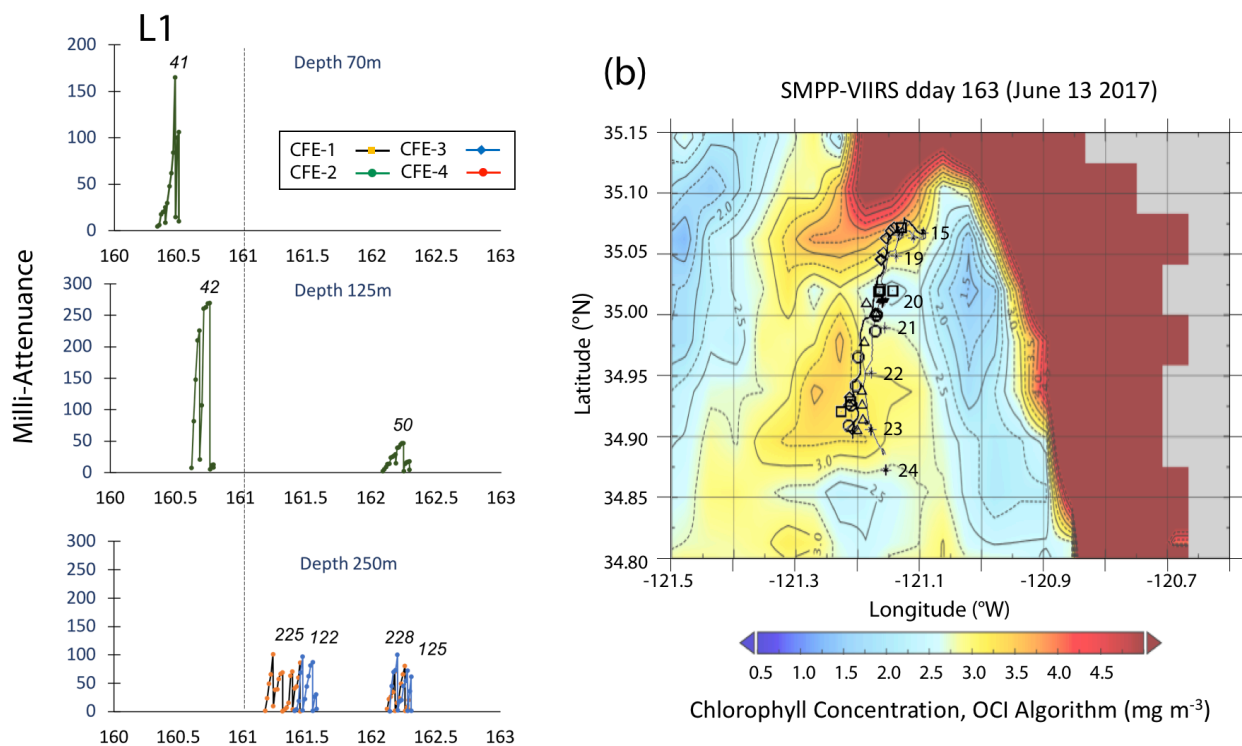


Figure A1-1. (a). Raw attenuance time series for CFEs deployed at L1 (300 m data not shown). See Fig. 2 for deployment context. Italicized numbers are CFE dive numbers. (b). Map showing deployment and trajectories of CFEs, CTD station locations, and tracks of the productivity drifter and sediment trap array during the intensive studies at L2. The overlay is the SMPP-VIIRS chlorophyll field for June 13 2017. CTD cast numbers are shown on the plot.

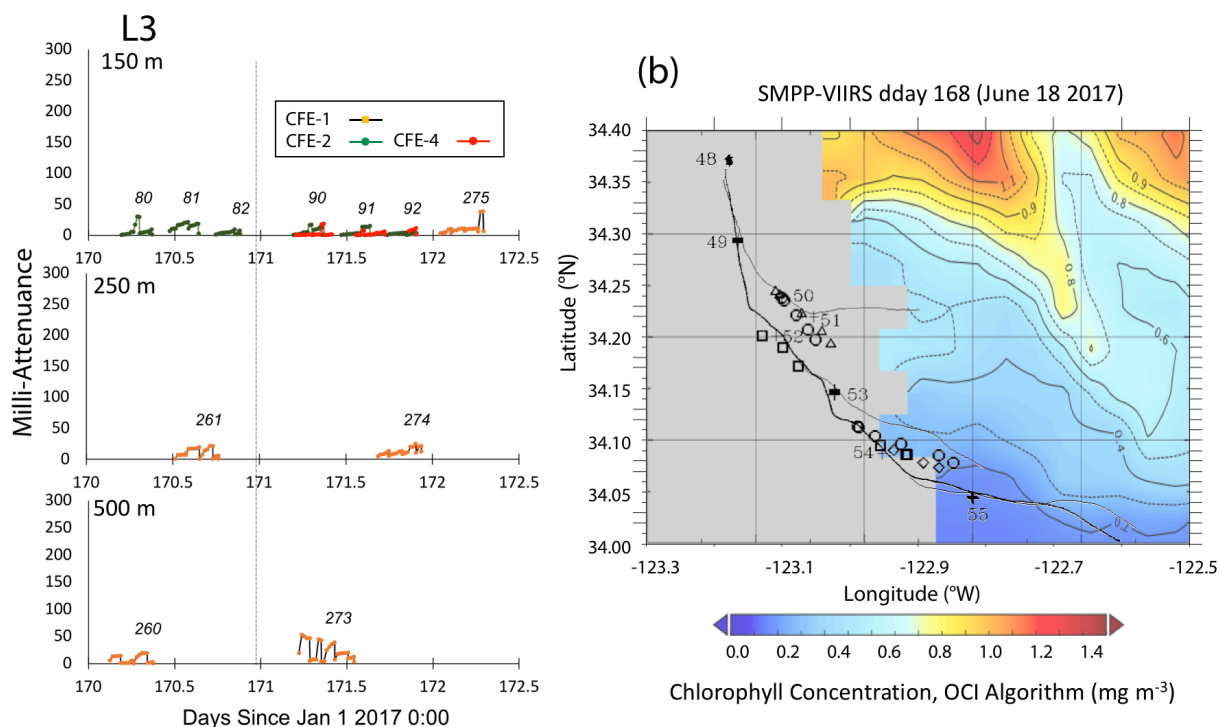


Figure A1-2. (a). Raw attenuation time series for CFEs deployed at L1 (300 m data not shown). See Fig. 2 for deployment context. Italicized numbers are the dive numbers corresponding to the data. **(b).** Map showing deployment and trajectories of CFEs, CTD station locations, and tracks of the productivity drifter and sediment trap array during the intensive studies at L2. The overlay is the SMPP-VIIRS chlorophyll field for June 18 2017 – prior to deployments. There is no contemporaneous imagery. CTD cast numbers are shown on the plot.

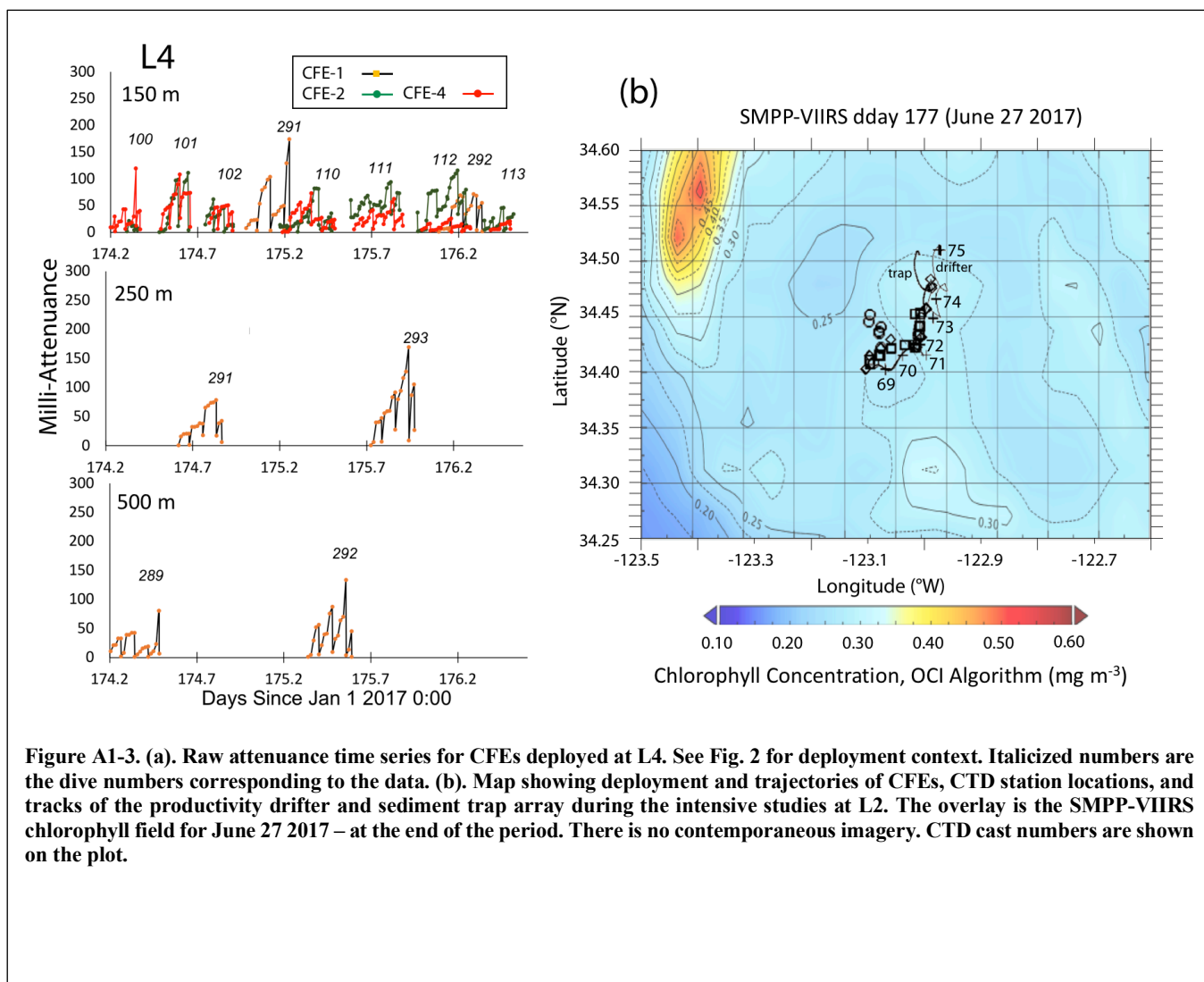


Figure A1-3. (a). Raw attenuation time series for CFEs deployed at L4. See Fig. 2 for deployment context. Italicized numbers are the dive numbers corresponding to the data. **(b).** Map showing deployment and trajectories of CFEs, CTD station locations, and tracks of the productivity drifter and sediment trap array during the intensive studies at L2. The overlay is the SMPP-VIIRS chlorophyll field for June 27 2017 – at the end of the period. There is no contemporaneous imagery. CTD cast numbers are shown on the plot.



1000

